The Company of Biologists

RESEARCH ARTICLE

A *Drosophila* toolkit for HA-tagged proteins unveils a block in autophagy flux in the last instar larval fat body

Tadayoshi Murakawa[1,2], Tsuyoshi Nakamura[1], Kohei Kawaguchi[1], Futoshi Murayama[2], Ning Zhao[3], Timothy J. Stasevich[3,4], Hiroshi Kimura[1,2,4] and Naonobu Fujita[1,2,5,*]

ABSTRACT

For *in vivo* functional analysis of a protein of interest (POI), multiple transgenic strains with a POI that harbors different tags are needed but generation of these strains is still labor-intensive work. To overcome this, we have developed a versatile *Drosophila* toolkit with a genetically encoded single-chain variable fragment for the HA epitope tag: 'HA Frankenbody'. This system allows various analyses of HA-tagged POI in live tissues by simply crossing an HA Frankenbody fly with an HA-tagged POI fly. Strikingly, the GFP-mCherry tandem fluorescent-tagged HA Frankenbody revealed a block in autophagic flux and an accumulation of enlarged autolysosomes in the last instar larval and prepupal fat body. Mechanistically, lysosomal activity was downregulated at this stage, and endocytosis, but not autophagy, was indispensable for the swelling of lysosomes. Furthermore, forced activation of lysosomes by fat body-targeted overexpression of Mitf, the single MiTF/TFE family gene in *Drosophila*, suppressed the lysosomal swelling and resulted in pupal lethality. Collectively, we propose that downregulated lysosomal function in the fat body plays a role in the metamorphosis of *Drosophila*.

KEY WORDS: HA epitope, *Drosophila*, Lysosome, Autophagy, Fat body, Development

INTRODUCTION

Protein functional analysis is fundamental in cell and developmental biology. Multiple transgenic strains with a protein of interest (POI) that harbors different tags are needed for *in vivo* functional analysis (Kanca et al., 2017), e.g. a transgenic line with an epitope tag-fused construct for immunostaining or immunoprecipitation (Vandemoortele et al., 2019), a GFP- or RFP-fused construct for live imaging (Dunst and Tomancak, 2019), a biotin ligase-fused construct for proximity labeling (Bosch et al., 2021), or a RFP-GFP tandem fluorescent-fused construct to monitor autophagic degradation in lysosomes (Kimura et al., 2007). Transgenesis methods introducing a tagged construct at a secondary site are well

established in *Drosophila* (Venken and Bellen, 2014). Nevertheless, it is still labor-intensive work to generate multiple transgenic strains for each gene of interest.

Autophagy, an intracellular degradation pathway in eukaryotes, is induced by environmental and developmental stimuli (Klionsky et al., 2021). Developmentally programmed autophagy is seen in a variety of *Drosophila* tissues, including the salivary gland, muscle and fat body (Fujita et al., 2017; Berry and Baehrecke, 2007; Rusten et al., 2004). It is thought that developmental autophagy allows the degradation and turnover of the cytosolic materials required for tissue remodeling during metamorphosis (Fujita et al., 2017). In the fat body, autolysosomes, a hybrid organelle of autophagosome and lysosome, are enlarged and accumulate massively at the last larval and white prepupal stage (Rusten et al., 2004; Butterworth et al., 1988; Butterworth and Forrest, 1984). The steroid hormone ecdysone, the master regulator of insect development, drives developmental autophagy in the fat body through downregulation of the Akt/PI3K axis (Rusten et al., 2004). However, it is unclear whether the robust induction of autophagy by ecdysone is the most important cause of the accumulation of enlarged autolysosomes. Autophagic flux has not yet been explored; therefore, it is still possible that a delay in autolysosome turnover results in the accumulation of enlarged autolysosomes in the last instar larval and prepupal fat body.

Here, we have developed a *Drosophila* toolkit of HA Frankenbody, a genetically encoded single-chain variable fragment for the HA epitope tag (Zhao et al., 2019). As the FlyORFeome project generates and distributes a comprehensive *in vivo* genome-wide UAS-ORF-3xHA library of *Drosophila* (Bischof et al., 2012), the HA Frankenbody toolkit is powerful for functional analysis of a POI. This tool has allowed us to carry out live-imaging of HA-tagged constructs in *Drosophila* tissues. By exploiting the pH sensitivity of GFP, GFP-mCherry tandem fluorescently tagged (TF) HA Frankenbody visualizes the autophagic degradation of HA-tagged proteins. Additionally, TF-tagged HA Frankenbody reveals a block in autophagic flux in the last instar larval and prepupal fat bodies, probably due to insufficient acidification of lysosomes. Altogether, a HA Frankenbody toolkit enables various protein localization and dynamics studies, including the autophagic degradation assay, by simply crossing HA Frankenbody transgenic flies, HA Frankenflies, with HA-tagged POI flies.

RESULTS

HA Frankenbody recognizes HA-tagged constructs in live *Drosophila* tissues

We generated a series of transgenic lines harboring fluorescent protein-fused HA Frankenbody under UAS or QUAS enhancer sequences (Table 1) to express the HA Frankenbody in *Drosophila* tissues. Binary expression systems allow the expression of genes in a tissue of interest (Brand and Perrimon, 1993; Riabinina et al.,

DEVELOPMENT

1

Table 1. Anti-HA Frankenflies

Category	Chromosome	Genotype
Transgenic lines	1;2	w; UAS-Frankenbody^{HA}:GFP (attP40)
	1;2	w; UAS-Frankenbody^{HA}:mCherry (attP40)
	1;2	w; UAS-Frankenbody^{HA}:GFP:mCherry (attP40)
	1;3	w; QUAS-Frankenbody^{HA}:GFP (attP2)
	1;3	w; QUAS-Frankenbody^{HA}:mCherry (attP2)
	1;3	w; QUAS-Frankenbody^{HA}:GFP:mCherry (attP2)
Combined lines	1;2	w; Cg-GAL4, UAS-Frankenbody^{HA}:GFP
	1;2	w; Cg-GAL4, UAS-Frankenbody^{HA}:mCherry
	1;2	w; Cg-GAL4, UAS-Frankenbody^{HA}:GFP:mCherry
	1;2;3	w; UAS-Frankenbody^{HA}:GFP; pnr-GAL4
	1;2;3	w; UAS-Frankenbody^{HA}:mCherry; pnr-GAL4
	1;2;3	w; UAS-Frankenbody^{HA}:GFP:mCherry; pnr-GAL4
	1;2;3	w; UAS-Frankenbody^{HA}:GFP; DMef2-GAL4
	1;2;3	w; UAS-Frankenbody^{HA}:mCherry; DMef2-GAL4
	1;2;3	w; UAS-Frankenbody^{HA}:GFP:mCherry; DMef2-GAL4
	1;2;3	w; UAS-Frankenbody^{HA}:GFP; da-GAL4
	1;2;3	w; UAS-Frankenbody^{HA}:mCherry; da-GAL4
	1;2;3	w; UAS-Frankenbody^{HA}:GFP:mCherry; da-GAL4

2015). To express both the HA-tagged protein and the HA Frankenbody construct under the control of the UAS sequences, the progenies need three transgenes: (1) a tissue-specific GAL4 driver; (2) a UAS gene of interest (GOI)-HA; and (3) a UAS-HA Frankenbody (Fig. 1A). For this purpose, the UAS-HA Frankenbody was combined with several GAL4 lines, such as Cg-GAL4, DMef2-GAL4, pnr-GAL4 or da-Gal4 (Table 1 and Fig. 1A). These are drivers for fat bodies, muscle cells, larval epidermal cells and broad tissues. We used larval epidermal cells (LECs) to assess the system because LECs are mononuclear and form a monolayer suitable for observing intracellular organelles. First, we expressed HA Frankenbody-GFP in the absence of HA-tagged protein. HA Frankenbody-GFP diffusely localized in both cytosol and nucleus, in the same way as GFP, in the absence of an HA-tagged construct (Fig. 1B; LacZ, control). Next, we co-expressed HA Frankenbody-GFP and HA-tagged organelle markers. γCOP, TOM20 and βTub97EF are markers for Golgi, mitochondria and microtubules, respectively. The localization of HA Frankenbody-GFP changed upon expression of γCOP-3xHA, TOM20-3xHA or βTub97EF-3xHA (Fig. 1B). HA Frankenbody-GFP signal colocalized entirely with the anti-HA immunostaining signal (Fig. 1B, magnified and line-plot). We also confirmed their colocalization in larval body wall muscles (LBWMs) (Fig. S1). These results show that the HA Frankenbody visualizes HA-tagged proteins in *Drosophila* tissues.

Next, we observed the HA Frankenbody-GFP in live tissues. HA Frankenbody-GFP and HA-tagged protein were co-expressed in LECs, LBWMs or fat bodies, and observed in live tissues by confocal microscopy (Fig. 2A-C, Fig. S2). LECs and LBWMs were observed through the cuticle in intact animals. Conversely, fat bodies were dissected, as they were too far from the cuticle for a high-magnification objective lens. Upon co-expression of 3xHA-tagged organelle markers, HA Frankenbody-GFP showed the typical localization pattern associated with each organelle (Fig. 2, Fig. S2). Collectively, HA Frankenbody allows imaging of HA-tagged constructs in live *Drosophila* tissues.

We have recently reported that the spinster-positive tubular autolysosomal (tAL) network functions in the remodeling of the abdominal muscles during metamorphosis (Murakawa et al., 2020). The tAL network is fragile and highly sensitive to dissection and fixation processes (Murakawa et al., 2020; Johnson et al., 2015).
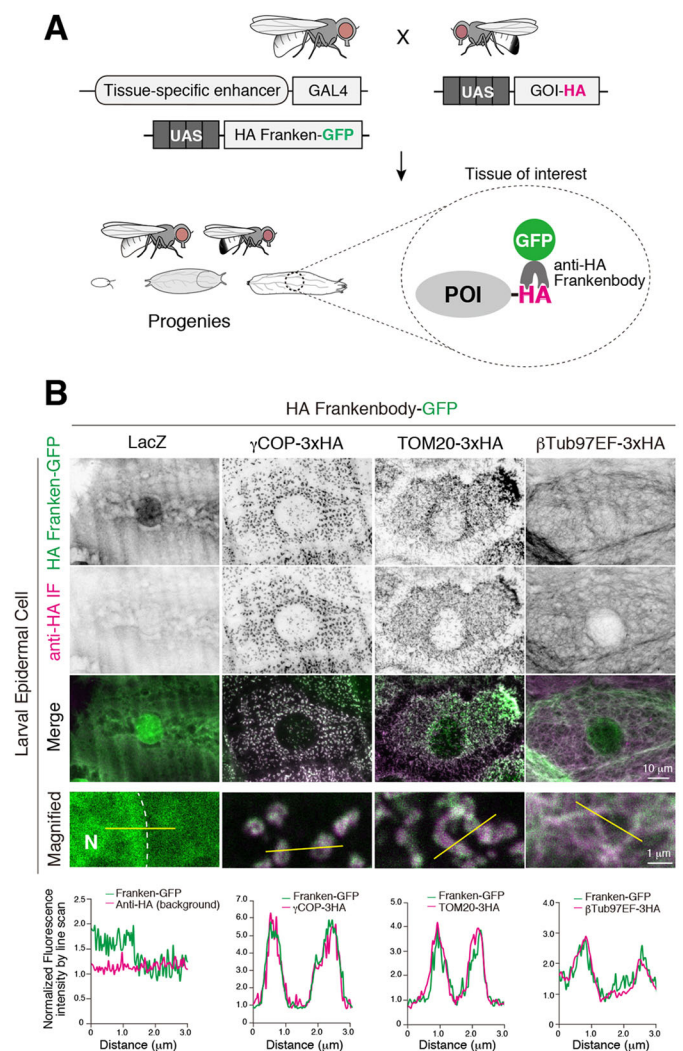

Fig. 1. HA Frankenbody recognizes HA-tagged protein in larval epidermal cells. (A) Schematic of the HA Frankenbody strategy using the GAL4-UAS binary expression system. (B) Colocalization of HA Frankenbody-GFP and γCOP-3xHA, TOM20-3xHA or βTub97EF-3xHA in larval epidermal cells. N, nucleus. Line plots profile the yellow line in each panel.
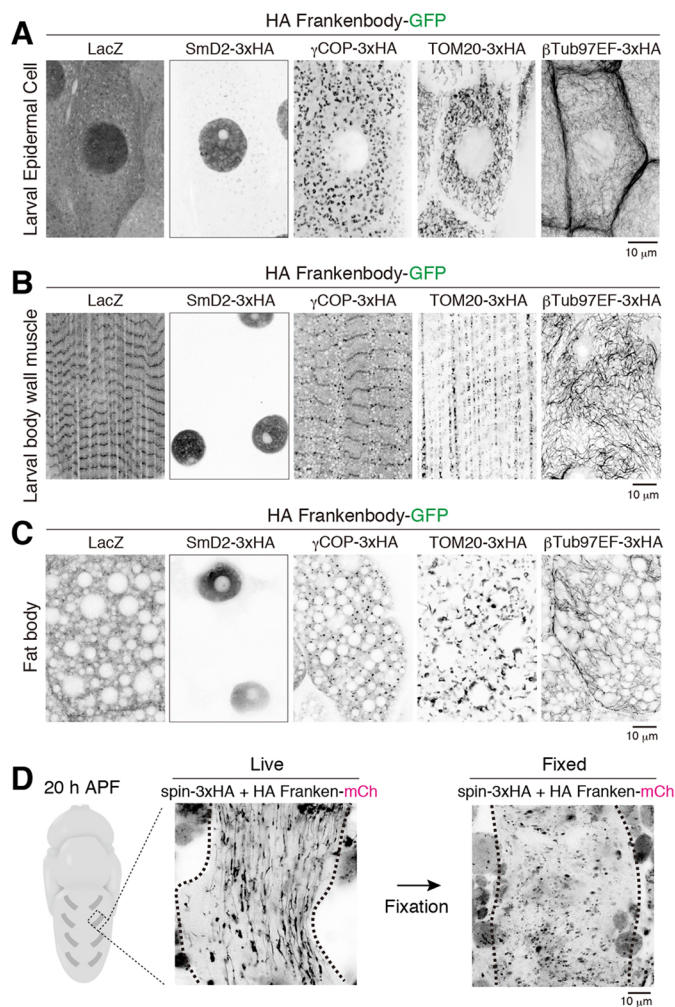
2

Fig. 2. HA Frankenbody allows imaging of HA-tagged constructs in live *Drosophila* tissues. (A-C) Localization of HA Frankenbody-GFP in cells expressing the indicated 3×HA-tagged constructs in live LECs (A), LBWMs (B) or fat bodies (C). (D) Pupal DIOMs expressing both spinster-3xHA and HA Frankenbody-mCherry were observed before (Live) and after (Fixed) fixation.

Hence, it is almost impossible to observe the tAL network by immunostaining. In contrast to that, HA Frankenbody-mCherry visualized the spin-3xHA-positive tAL network in 20 h after puparium formation (APF) dorsal internal oblique muscles (DIOMs) (Fig. 2D). Subsequent to dissection and fixation, the structure was lost (Fig. 2D), showing that HA Frankenbody is suitable for imaging of fragile structures that are highly sensitive to fixation.

TF-tagged HA Frankenbody visualizes the lysosomal degradation of HA-tagged proteins of interest

The tandem fluorescent protein-tagged Atg8 homolog, GFP-mCherry-LC3/Atg8, allows the assessment of autophagy flux because of the pH sensitivity of GFP (Kimura et al., 2007). Analogous to this reporter, we generated a transgenic fly carrying UAS-HA Frankenbody-GFP-mCherry (Table 1) to monitor the autophagic degradation of HA-tagged protein. Both GFP and mCherry fluoresce at the neutral pH of the cytosol (Fig. 3A left). On the other hand, only mCherry fluoresces at the acidic pH in lysosomes because the pKa is around 6.0 for GFP, and it is quenched in acidic conditions (Fig. 3A right). To validate the TF system, both HA Frankenbody-TF and HA-tagged constructs were

expressed in the larval fat bodies. Third instar larvae (3IL) were fed or starved for 4 h, and fat bodies were observed (Fig. 3B,C). In fed condition, expression of LacZ, GAPDH1-3xHA or TOM20-3xHA induced only a low level of mCherry-single-positive puncta (Fig. 3B,C). In contrast, expression of HA-ref(2)p, an established autophagy cargo protein (Komatsu et al., 2007; Nezis et al., 2008), induced robust formation of mCherry-single-positive puncta, suggesting HA-ref(2)p is degraded in the lysosome even under fed conditions (Fig. 3B,C). We obtained a similar result in 1-week-old adult indirect flight muscles (Fig. S3A,B). Furthermore, nutrient starvation significantly elevated the lysosomal degradation of the TF-tagged HA Frankenbody (Fig. 3B,C). We confirmed that the mCherry-single-positive puncta were colocalized well with LysoTracker dye and Cathepsin L (Fig. S3C). These results indicate that mCherry accumulated in the acidic lysosomal compartments.

To examine whether the degradation of the TF reporter depends on autophagy, we used the *Atg5* null to examine the formation of mCherry-single-positive puncta in the fat body co-expressing HA-ref(2)p and HA Frankenbody-TF. *Atg5* is an essential gene for autophagy (Mizushima et al., 1998; Kim et al., 2016). As shown in Fig. 3D,E, loss of *Atg5* significantly blocked mCherry-single-positive puncta formation. We further confirmed that the degradation of HA Frankenbody-TF depended on autophagy even in the absence of HA-fused construct (Fig. S3D,E).

We noticed that, under fed conditions, HA-ref(2)p expression caused the bright spherical structures positive for both GFP and mCherry (Fig. 3B,D, Fig. S4A), and the number and size of the GFP-positive spherical structures significantly decreased in parallel with their degradation upon starvation (Fig. 3D,E, Fig. S4A,B). In addition, the Frankenbody-TF-positive spherical structures were negative for Lysotracker dye (Fig. S4C). These results indicate that the spherical structures are not lysosomal compartments but liquid or gel-like ref(2)p-droplets in the cytosol (Pircs et al., 2012; Kageyama et al., 2021).

Next, we examined whether HA Frankenbody-TF expression triggers degradation of HA-fused constructs. In the starved larval fat bodies, HA Frankenbody-TF expression had little noticeable effect on the protein level of GAPDH1-3xHA or TOM20-3xHA (Fig. S5A,B). In contrast, the level of HA-ref(2)p was elevated by HA Frankenbody-TF expression (Fig. S5C), suggesting that HA Frankenbody-TF stabilizes HA-ref(2)p. To test whether the stabilization depends on autophagy, we examined the loss of *Atg5* on HA-ref(2)p level in the presence or absence of HA Frankenbody-TF. The elevation of HA-ref(2)p induced by HA Frankenbody-TF was not dependent on *Atg5* (Fig. S5D), indicating that HA-ref(2)p is stabilized in an autophagy-independent mechanism. Furthermore, it has been shown that p62/ref(2)p is also degraded by the ubiquitin-proteasome system (Song et al., 2016). Therefore, it is plausible that HA Frankenbody-TF binds and stabilizes HA-ref(2)p through protection from the ubiquitin-proteasome system. Altogether, the above results demonstrate that the HA Frankenbody-TF visualizes the lysosomal degradation of HA-tagged protein of interest in *Drosophila* tissues.

Lysosomal function is developmentally regulated in the prepupal fat body

By using time course microscopy to observe fat bodies expressing HA Frankenbody-TF from early 3IL to white prepupa, we found that both GFP and mCherry fluoresce in the enlarged structures in the white prepupal fat bodies (Fig. 4A-C, white dotted circle in B). For quantification, the bright spherical structures positive for both
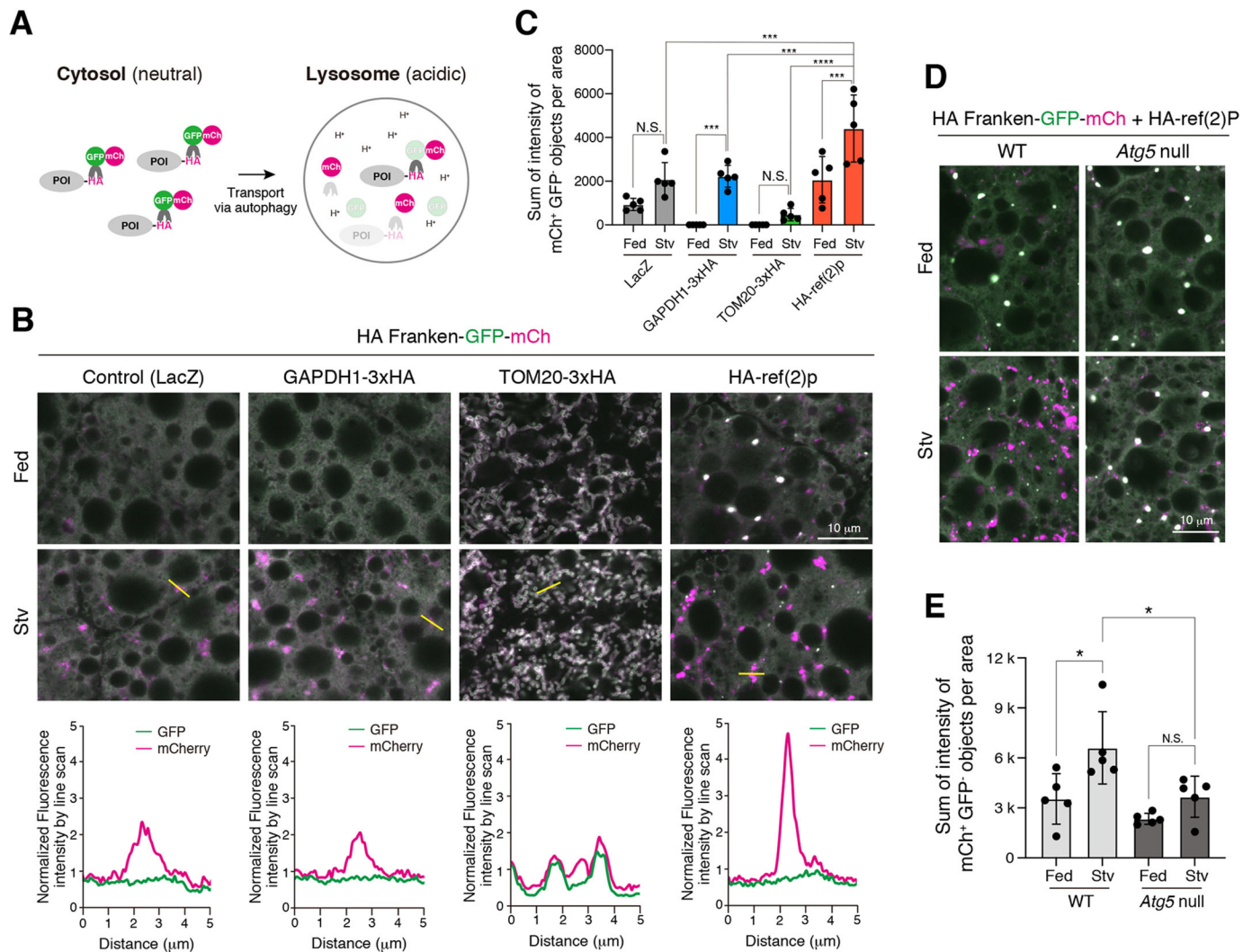
Fig. 3. TF-tagged HA Frankenbody visualizes the autophagic degradation of HA-tagged proteins of interest. (A) Schematic of the lysosomal degradation assay using TF-tagged HA Frankenbody. (B,C) Early 3IL larvae expressing HA Frankenbody-GFP-mCherry and the indicated HA-tagged construct in fat bodies were fed or starved for 4 h. (B) Confocal images of GFP and mCherry channels in each condition. Line plots profile the yellow line in each panel. (C) Quantification of the total intensity of mCherry-positive and GFP-negative objects per area±s.d. for five images from five animals (Sidak's test). (D,E) Effect of the loss of *Atg5* on the degradation of HA Frankenbody-GFP-mCherry in the fat body co-expressing HA-ref(2)p. (D) Confocal images of GFP and mCherry channels in each condition. (E) Quantification of the total intensity of mCherry-positive and GFP-negative objects per area±s.d. for five images from five animals (Sidak's test).

GFP and mCherry were excluded (Fig. 4B, cyan arrowhead) because they were LysoTracker-negative liquid or gel-like ref(2)p-droplets (Fig. S4, Fig. 3D,E). Parallel to the increase of GFP and mCherry double-positive objects, the number of mCherry-single-positive objects decreased (Fig. 4B,C, white arrowhead). These results suggest that the GFP and mCherry double-positive structures are lysosome-related structures with relatively higher pH. To test this possibility, white prepupal fat bodies expressing both HA Frankenbody-TF and HA-ref(2)p were stained with LysoTracker Deep Red: a dye for acidic organelles. As shown in Fig. 4D, the enlarged GFP and mCherry double-positive structures were also positive for LysoTracker dye, indicating that they are acidic lysosomal compartments. Although the LysoTracker probe accumulates and fluoresces in the acidic compartments, its intensity is largely independent of pH (Guha et al., 2014). In contrast, the LysoSensor dye exhibits a change in fluorescent intensity with luminal pH. Therefore, we compared the intensity of LysoSensor Green in the compartments in starved 3IL or white

prepupal fat bodies. The LysoSensor showed a significantly lower intensity in the white prepupal fat body than the starved 3IL fat body (Fig. 4E,F), indicating that lysosomal acidification is regulated in the prepupal fat bodies. We further confirmed that lysosomal protease activity, as monitored by Magic Red, also decreased more in the white prepupal fat body than it did in the starved 3IL fat body (Fig. 4G,H). From these results, we conclude that lysosomal function is developmentally downregulated in the white prepupal fat body.

Lysosomal function is developmentally downregulated in an autophagy-independent manner

It is thought that robustly induced autophagy is the dominant cause of the enlargement of lysosomal compartments in the last instar larval fat body (Rusten et al., 2004). To test this model, we examined whether there was a correlation between autophagy induction and the size of the lysosome. The number of GFP-Atg8 puncta (autophagosomes) and the size of LysoTracker Red-positive
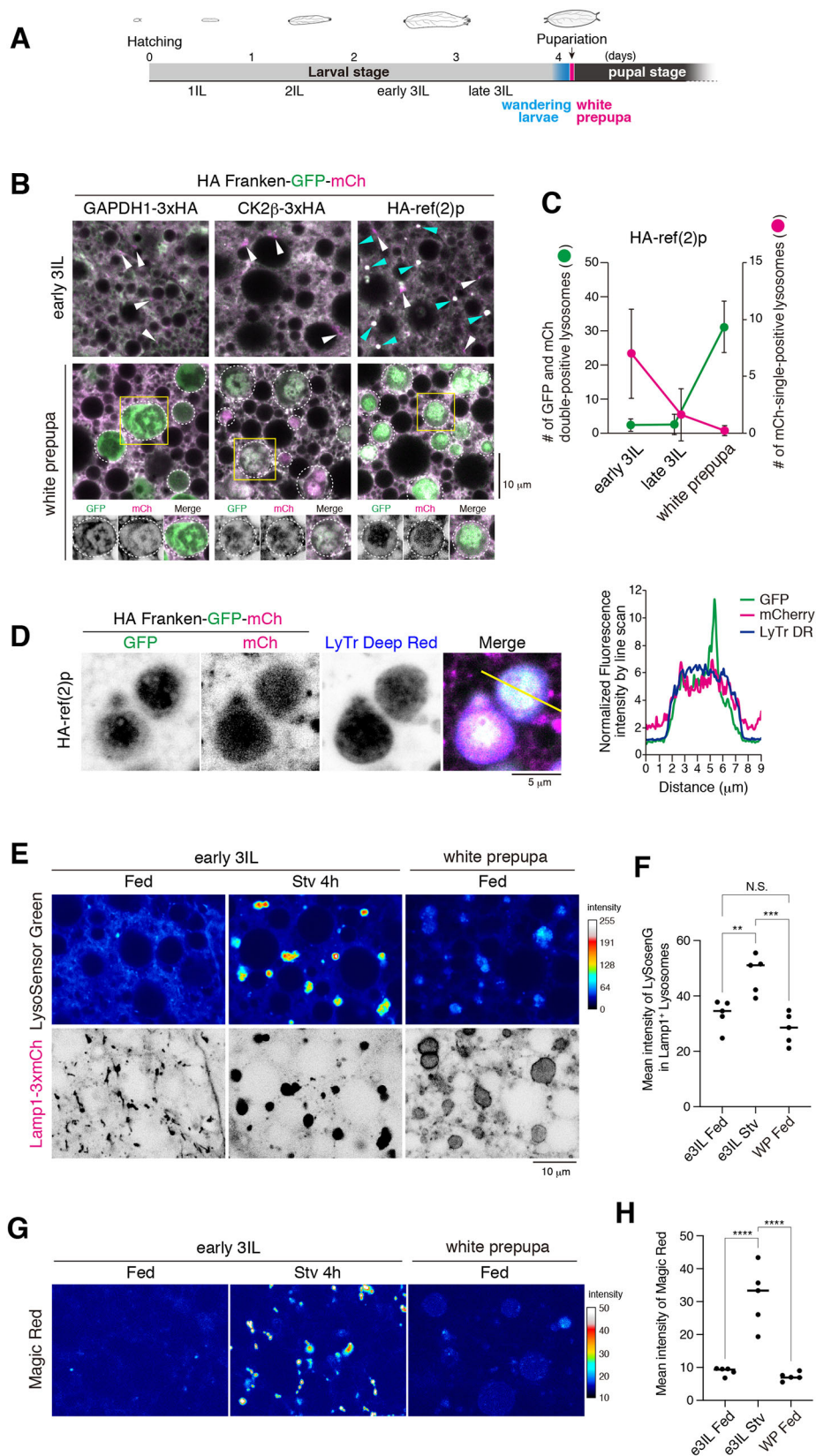
Fig. 4. Acidification of lysosomes in the prepupal fat body is regulated. (A) Timeline of fly development from embryo to pupa at 25°C. (B,C) Fat bodies expressing both HA Frankenbody-GFP-mCherry and GAPDH1-3xHA, CK2β-3xHA or HA-ref(2)p at the early 3IL or pupariation (white prepupa). (B) Confocal images of GFP and mCherry channels under the indicated conditions. mCherry-single-positive puncta, white arrowhead; both GFP and mCherry double-positive bright spherical structures, cyan arrowhead; both GFP and mCherry double-positive enlarged structures, white dotted circle. The cropped single channels are inverted images of black and white. The enlarged green-looking lysosomes are also positive for mCherry. (C) The number of objects positive for only mCherry (pink) or positive for both GFP and mCherry (green). (D) Colocalization of GFP, mCherry and LysoTracker Deep Red in white prepupal fat body expressing both HA Frankenbody-GFP-mCherry and HA-ref(2)p. Line plots profile the yellow line in the panel. (E,F) LysoSensor Green staining of fat bodies expressing Lamp1-mCherry at early 3IL or pupariation (white prepupa). (E) The intensity map shows a representative image of the intensities of LysoSensor Green-positive objects. (F) Quantification of mean intensities of Lysosensor Green-positive objects. $n=5$ (Tukey's test). (G,H) Fat bodies were stained with Magic Red at early 3IL or pupariation (white prepupa). (G) The intensity map shows a representative image of the intensities of Magic Red-positive objects. (H) Quantification of mean intensities of MagicRed-positive objects ($n=5$) (Sidak's test). Scale bar in E also applies to G.

compartments (lysosomes) were quantified in starved 3IL or white prepupal fat bodies (Fig. 5A-D) (Kabeya et al., 2000). The ratio of the lysosome area per number of autophagosomes was significantly higher at the white prepupal stage than at the starved 3IL stage (Fig. 5D), suggesting that not only autophagy induction but also other mechanisms contribute to the enlargement of lysosomes. Next, we tested the loss of *Atg5* on the size of Lamp1-3xmCherry-positive lysosomes, to examine further the contribution of
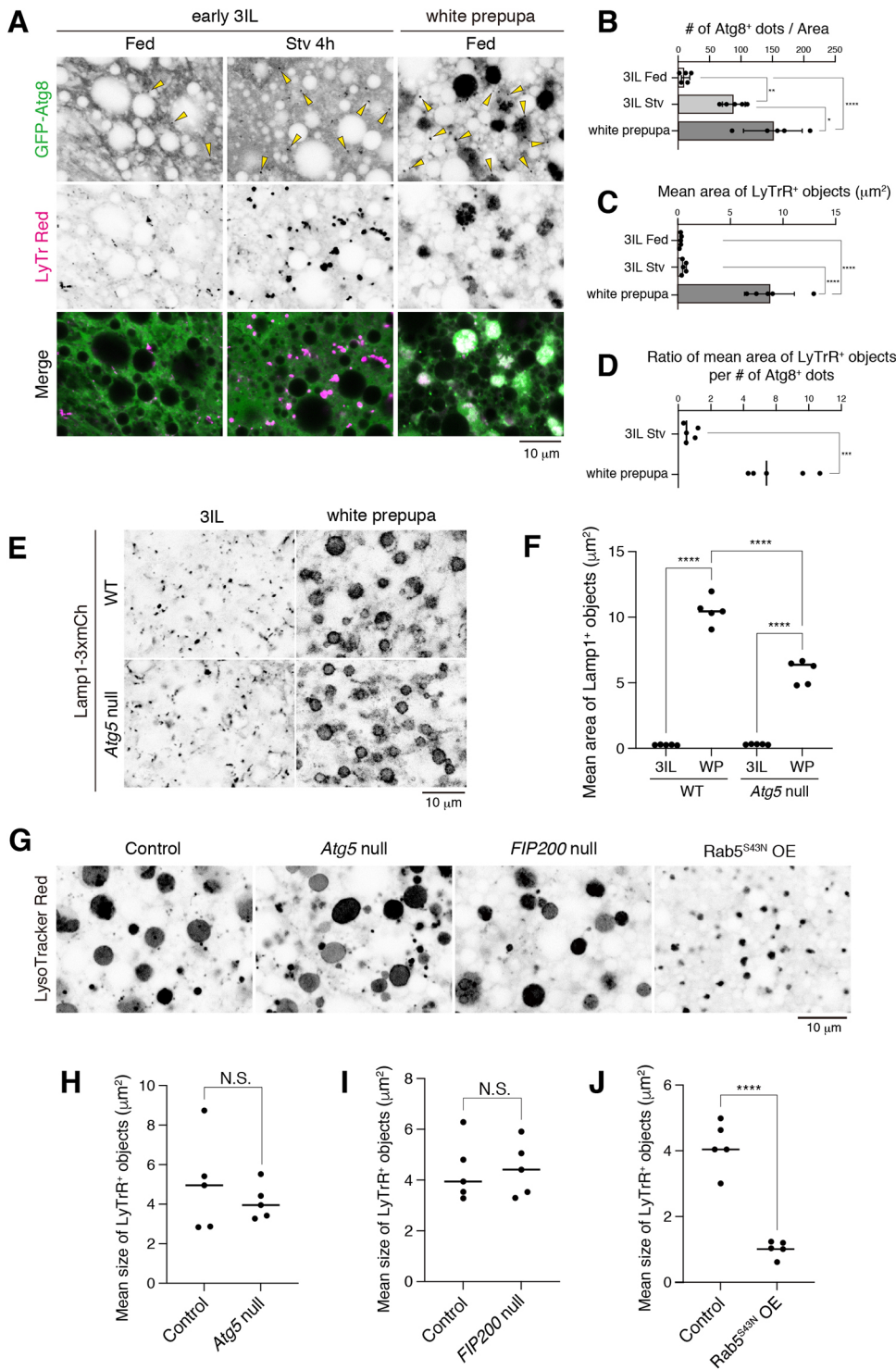
Fig. 5. Lysosomes are developmentally downregulated in an autophagy-independent manner. (A-D) Fed or starved fat bodies expressing GFP-Atg8 were stained with LysoTracker red at early 3IL or pupariation (white prepupa). (A) Confocal images of GFP-Atg8 and LysoTracker red under the indicated conditions. GFP-Atg8-positive small puncta, yellow arrowhead. (B) The number of small GFP-Atg8 dots per area (Tukey's test). (C) Mean area of LysoTracker red-positive objects (Tukey's test). (D) The ratio of the area of LysoTracker red-positive objects per number of small GFP-Atg8 dots±s.d. for five images from five animals (Sidak's test). (E,F) Effect of loss of *Atg5* on the size of lysosomes at early 3IL or pupariation (white prepupa). (E) Confocal images of Lamp1-3xmCherry under the indicated conditions. (F) The mean area of Lamp1-3xmCherry-positive objects±s.d. for five images from five animals (Sidak's test). (G-J) The effect of loss of *Atg5* or *FIP200*, or Rab5^{S43N} overexpression on the size of lysosomes in the white pupal fat bodies. (G) Confocal images of LysoTracker Red-positive lysosomes in the white prepupal fat bodies. (H-J) The mean area of LysoTracker Red-positive objects±s.d. for five images from five animals (unpaired *t*-test).

autophagy to the enlargement of lysosomes (Hegedűs et al., 2016). Strikingly, the enlargement was observed even in *Atg5*-null conditions (Fig. 5E-F). The size of the lysosomes was affected only modestly by the loss of *Atg5* in the white prepupal fat body. Next, we performed a flux assay using chloroquine, a well-known lysosomotropic agent that increases lysosomal pH and induces vacuolation (Zhou et al., 2020). Chloroquine feeding significantly increased the size of the Lamp-positive lysosomes in white prepupal LECs (Fig. S6A-C). In sharp contrast, chloroquine feeding did not induce the enlargement of lysosomes nor the decrease in lysosomal

protease activity in the fat body at the same stage (Fig. S6A,B,D-F), suggesting lysosomal function is downregulated in the white prepupal fat body.

Which trafficking pathway does play a role in the enlargement of lysosomes? Besides autophagy, endocytic pathways also deliver cargoes to the lysosomes: therefore, we tested temporal blockade of endocytosis on the enlargement of lysosomes. For this purpose, Rab5^{S43N}, a dominant-negative mutant of Rab5, was temporally expressed in the late larval fat body by Lsp2-GAL4 (Cherbas et al., 2003). Consistent with Fig. 5E, loss of *Atg5* or *FIP200/Atg17*
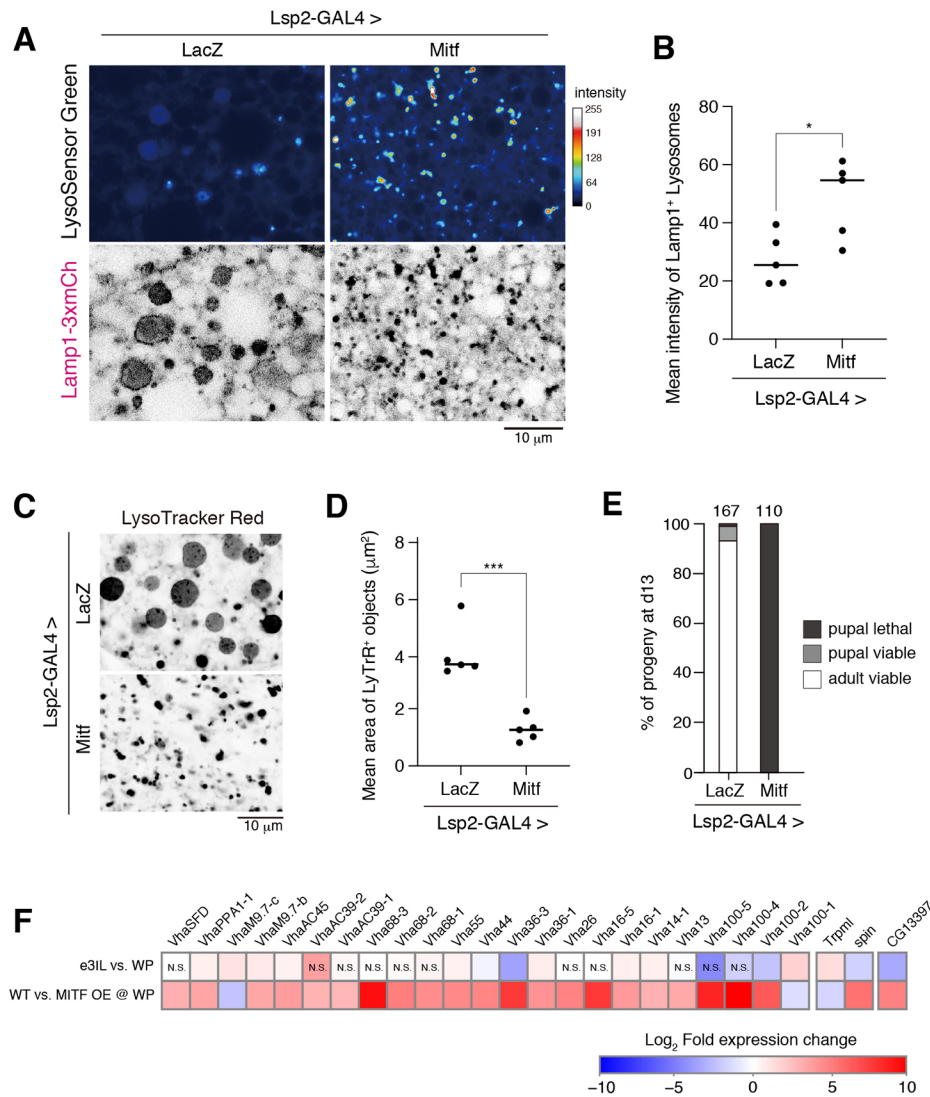
Fig. 6. Forced activation of lysosomes by Mitf overexpression in the white prepupal fat bodies. (A,B) LysoSensor Green staining of white prepupal fat bodies overexpressing LacZ (control) or Mitf. (A) The intensity map shows a representative image of the intensities of LysoSensor Green-positive objects. (B) Quantification of mean intensities of LysoSensor Green in Lamp1-3xmCherry-positive objects (n=5) (unpaired t-test). (C,D) The effect of Mitf overexpression on the size of LysoTracker Red-positive lysosomes in white prepupal fat bodies. (C) Confocal images of LysoTracker Red in white prepupal fat bodies expressing LacZ (control) or Mitf (unpaired t-test). (D) The mean area of LysoTracker Red-positive objects±s.d. for five images from five animals. (E) Percentage of viable and lethal progeny 13 days after egg laying with fat body-targeted Mitf overexpression. (F) Heat map illustrating RNA-Seq differential expression data of fat bodies. Pairwise comparisons are shown for each combination. Top row, early 3IL fat body versus white prepupal fat body. The score of white prepupa was divided by that of early 3IL. Bottom row, control white prepupal fat body versus white prepupal fat body overexpressing Mitf. The score of Mitf overexpressing sample was divided by that of control (n=3). Non-significant differences with P>0.1 are indicated (N.S.).

hardly affected the size of LysoTracker Red-positive lysosomes (Fig. 5G,H,I). In sharp contrast, Rab5^{S43N} overexpression significantly reduced the size of lysosomes (Fig. 5G,J). These results show that endocytosis, but not autophagy, contributes dominantly to the enlargement of lysosomes in the prepupal fat body.

We explored the biological significance of the downregulation of lysosomes in the fat body. For this purpose, we tested fat body-targeted Mitf overexpression by Lsp2-GAL4 on the enlargement of lysosomes and the development of *Drosophila*. Mitf is the single MiTF/TFE family gene in *Drosophila* and is a master regulator of the autophagy-lysosome pathway (Zhang et al., 2015; Bouché et al., 2016). Thus, Mitf overexpression upregulates lysosomal functions through transcription activation of a series of lysosome-related genes, including v-ATPase subunits required for the acidification of lysosomes (Bouché et al., 2016). We confirmed the transcriptional activation of lysosome-related genes by Mitf overexpression in the white prepupal fat body (Fig. 6F, bottom row). Mitf overexpression markedly suppressed the increase in lysosome pH and the enlargement of lysosomes in the white prepupal fat body (Fig. 6A-D), probably through the forced activation of lysosomes. It is important to note that Lsp2-GAL4 drives expression only after late 3IL. At 13 days after egg laying, almost all progenies became adults in control (Fig. 6E). By contrast, fat body-targeted Mitf

overexpression induced severe lethality at the pupal stage (Fig. 6E). The Mitf overexpression-induced lethality was independent of *Atg9*, an essential gene for autophagy (Wen et al., 2017) (Fig. S7), indicating that autophagy is not involved in the Mitf-induced lethality. These data suggest that the downregulation of lysosomes in the last instar larval and white prepupal fat body plays a role in the metamorphosis of *Drosophila*.

Last, we performed a comparative RNA-seq to explore transcriptional regulation of lysosome-related genes in the fat body. As shown in Fig. 6F, the mRNA level of several lysosome-related genes, including v-ATPase subunits, spinster and lysosomal α-N-acetylglucosaminidase (CG13397), significantly dropped in the white prepupal fat body compared with 3IL fat body. As it is known that hypofunction of them leads to lysosomal dysfunction and swelling (Dermaut et al., 2005; Rigon et al., 2021), their transcriptional downregulation might be a key to understanding the developmental regulation of lysosomes in the fat body.

DISCUSSION
A toolkit of HA Frankenbody allows a versatile localization and dynamic analysis of HA-tagged POIs in *Drosophila*. A combination of HA Frankenflies and the Zurich FlyORFeome library enables large-scale localization screening *in vivo*. The FlyORFeome project

aims to develop a comprehensive *in vivo* genome-wide UAS-ORF library. Notably, the UAS-transgenes were fused with a 3xHA tag at the C terminus (Bischof et al., 2012). Figs 1 and 2 demonstrate that our strategy is powerful enough for *in vivo* subcellular localization analysis. Cytosolic HA Frankenbody does not recognize the HA tag exposed in the luminal or extracellular space. However, we think this feature is advantageous for analyzing the membrane topology of a POI. If an inserted HA tag is recognized by HA Frankenbody, one can tell that the HA-fused segment is exposed to the cytosol.

Immunostaining is a standard protocol for the localization analysis of epitope-tag fused constructs. Nevertheless, chemical fixation and permeabilization by detergents often cause artifacts such as changes in the morphology of organelles, loss of epitopes or mislocalization of proteins (Richter et al., 2018). As such, we analyzed the tAL network, which is highly sensitive to a normal immunostaining process (Murakawa et al., 2020). A combination of spin-3xHA and HA Frankenbody-mCherry succeeded in imaging this tubular network in live muscle cells (Fig. 2D). Hence, the HA Frankenbody system is especially suitable for fragile structures labeled with HA-tagged POI where fluorescent protein-tagging is not a viable option.

TF-tagged HA Frankenbody enables monitoring of autophagic degradation of HA-fused POI in lysosomes (Fig. 3). HA-ref(2)p, a fly homolog of p62/SQSTM1 that is an established autophagy cargo, was more efficiently degraded compared with other constructs in both muscles and fat bodies (Fig. 3B,C and Fig. S3A,B). We also confirmed that the degradation of HA-ref(2)p depends on autophagy (Fig. 3D,E). Using a combination of TF-tagged HA Frankenbody and HA-fused FlyORF library allows the assessment of autophagic degradation of POIs without establishing a new tandem-fluorescent protein-fused transgenic line. Autophagy specifically sequesters target organelles, including ER, mitochondria, peroxisomes and lysosomes, for degradation (Morishita and Mizushima, 2019); however, the physiological roles of the organelle-phagy are not fully understood, especially in multicellular organisms. Thus, it would be interesting to examine the degradation of markers for each organelle in various tissues, developmental stages and nutrient conditions by the TF-tagged HA Frankenbody strategy. in addition, TF-tagged HA Frankenbody is a powerful tool for exploring cargo specificity in autophagy. Most selective autophagy cargoes have a short linear sequence motif, called LIR, LRS or AIM, that physically interacts with Atg8 family proteins (Kalvari et al., 2014). It is now feasible to test all predicted AIM-containing proteins by combining TF-tagged HA Frankenbody and the FlyORF library. A systematic approach would provide insights into cargo recognition by Atg8 on the autophagic membrane.

We observed accumulated and enlarged autolysosomes in the last instar larval and white prepupal fat body, consistent with previous reports (Rusten et al., 2004; Butterworth et al., 1988; Butterworth and Forrest, 1984). However, we propose here a new mechanistic model explaining this phenomenon. Our data support a model where decreased autophagic flux is the dominant cause of autolysosome accumulation. First, lysosomal acidification was downregulated in prepupal fat bodies (Fig. 4E,F). Second, blockade of lysosomal activity by chloroquine feeding did not significantly affect the size and activity of lysosomes at this stage (Fig. S6). Third, autophagy was dispensable for the enlargement of lysosomes (Fig. 5E-G), indicating that lysosomal activity is developmentally downregulated in an autophagy-independent manner.

The next question to be addressed is the mechanism of the downregulation of lysosomal activity in the last instar larval and prepupal fat body. As lysosomal acidification was altered compared with the early 3IL stage (Fig. 4E,F), the expression level of *vha* genes, encoding v-ATPase subunits required for lysosomal acidification, or assembly of V0 and V1 V-ATPase subcomplex, could be attenuated (Collins and Forgac, 2020). The regulation of lysosomal pH is complex, and it could be affected by anions, cations, membrane voltage, lysosomal lipids, etc. (Mindell, 2012; Sillence, 2013). Therefore, it is possible that the expression of other lysosome-related genes, such as *spinster*, is developmentally regulated in the fat body (Dermaut et al., 2005). To test the possibilities, we performed a comparative RNA-seq of 3IL and white prepupal fat bodies. We predict that Mitf is dispensable for the downregulation of lysosomes in the fat body, because most of the genes regulated by Mitf were not transcriptionally affected in the white prepupal fat body (Fig. 6F). The mRNA levels of several *vha* genes, *spinster* and lysosomal α-N-acetylglucosaminidase (CG13397) were significantly decreased in white prepupal fat bodies (Fig. 6F). CG13397 is a fly homolog of human α-N-acetylglucosaminidase that is a causative gene of Mucopolysaccharidosis type IIIB – a lysosomal storage disorder (Rigon et al., 2021). Further studies are needed to address whether the transcriptional regulation contributes to the enlargement of lysosomes in the last instar and white prepupal fat body.

Rab5-mediated endocytosis was indispensable for the swelling of lysosomes (Fig. 5G,J). Therefore, it is also possible that increased endocytic flux to lysosomes is a driver of the enlargement to some extent. It should be examined whether the endocytic activity is upregulated more in the white prepupal fat body than in the 3IL fat body. However, this is challenging because lysosomal activity is significantly decreased in the white prepupal fat body. Alternatively, an elevated basic metabolite could cause the downregulation of lysosomes. Metabolome analysis of early 3IL and white prepupal fat bodies would provide valuable clues to the mechanism behind the lysosomal swelling.

What is the biological significance of the block in autophagic flux in fat bodies? Forced activation of lysosomes by Mitf overexpression suppressed the accumulation of enlarged lysosomes in the fat body (Fig. 6C,D). Moreover, Mitf overexpression in the last instar larval fat body induced severe lethality at the pupal stage (Fig. 6E), although its precise mechanism has not yet been revealed. These results suggest that the downregulation of lysosomes in the fat body has a beneficial role in *Drosophila* development. Therefore, we hypothesize that the last instar larvae store autolysosomes in fat bodies as a nutrient source for the next harsh starvation period: the pupal stage. The accumulated autolysosomes in the larval fat body might be degraded and recycled in the pupal stage. Supporting this idea, time-course electron microscopy of the fat body showed that the number of autophagic vacuoles peaked at 1 day APF and then decreased during the remainder of metamorphosis (Butterworth et al., 1988). Alternatively, degradation of endocytosed hemolymph proteins or plasma membrane proteins in the fat body may have some kind of deleterious effect, and the ecdysone hormone blocks their degradation for proper development. The exciting questions to be explored are: (1) what are the dynamics of the enlarged autolysosomes in the pupal fat body?; (2) what is the effect of forced blockade of autolysosome turnover throughout the pupal period?; and (3) what is the mechanism of how fat body-targeted Mitf overexpression induces pupal lethality?

Besides the utilities described in this paper, HA Frankenbody could be applied to proximity labeling of HA-tagged POI by HA Frankenbody-APEX2 or BioID (Bosch et al., 2021) and

visualization of HA-POI in the extracellular space *in vivo* by a secreted form of HA Frankenbody, etc. Our study provides a new platform for the functional analysis of HA-tagged proteins *in vivo*. This strategy will be widely used, contributes to the fly community, and is also being applied to *in vivo* studies in other model organisms, such as worms, amphibians, zebrafish, plants and mice.

MATERIALS AND METHODS
Reagents and antibodies
The following antibodies were used: mouse anti-HA (1:1000; clone TANA2; M180-3, MBL), rabbit polyclonal anti-GFP (1:1000; 598, MBL), mouse anti-insect Cathepsin L (1:200; clone 193702; MAB22591, R&D Systems), anti-mouse IgG Alexa Fluor 594 conjugate (1:400; A11005, Thermo Fisher Scientific), anti-mouse IgG Alexa Fluor 405 conjugate (1:400; A48255, Thermo Fisher Scientific), HRP-conjugated AffiniPure goat anti-mouse IgG (1:10,000; 115-035-166, Jackson ImmunoResearch), HRP-conjugated AffiniPure goat anti-rabbit IgG (1:10,000; 111-035-144, Jackson ImmunoResearch), LysoTracker Red DND-99 (Thermo Fisher Scientific), LysoTracker Deep Red (Thermo Fisher Scientific), Lysosensor Green DND-189 (Thermo Fisher Scientific), Magic Red Cathepsin B assay kit (ImmunoChemistry Technologies) and Chloroquine diphosphate (TCI).

Drosophila strains
Flies were reared at 25°C unless otherwise stated. For tissue-targeted gene expression, the following drivers were used: DMef2-GAL4 for muscle, Cg-GAL4 for the fat body, pnr-GAL4 for larval epidermal cells and da-GAL4 for broad tissues. UAS-*LacZ* was used as a control. Genotypes are described in Table S1. All genetic combinations were generated by standard crosses. Genotypes of flies used in this study include the following: (1) *Atg5⁵ᶜᶜ⁵/FM7 actin-GFP* (from J. H. Lee, University of Michigan, Ann Arbor, MI, USA; *Atg5* null), (2) *endo_promoter-Lamp:3xmCherry1-9M* (from G. Juhasz, Hungarian Academy of Sciences, Budapest, Hungary), (3) *pnr-GAL4* (from D. Umetsu, Tohoku University, Sendai, Japan), (4) *w; UAS-HA:Ref(2)P_7M/TM3 Sb* (from S. Loh, University of Cambridge, UK), (5) *y w; UAS-GFP:Atg8a* (from T. Neufeld, University of Minnesota, Minneapolis, USA), (6) *w; UAS-Mitf* (96E) (from F. Pignoni, Upstate Medical University, Syracuse, NY, USA), (7) *w¹¹¹⁸; P{w⁺ᵐᶜ=Cg-GAL4.A}2* (Bloomington *Drosophila* Stock Center, BL7011; *Cg-GAL4*), (8) *y¹ w*; P{w⁺ᵐᶜ=GAL4-Mef2.R}3* (BL27390; *DMef2-GAL4*), (9) *w¹¹¹⁸; P{w⁺ᵐᶜ= UAS-lacZ.B}Bg4-1-2* (BL1776; *UAS-LacZ*), (10) *y w; P{w[+mC]=Lsp2-GAL4.H}3* (BL6357; Lsp2-GAL4), (11) *UAS-Smd2:3xHA* (FlyORF, Zurich ORFeome project, F003874), (12) *UAS-γCOP:3xHA* (F000931), (13) *UAS-βTub97EF:3xHA* (F001206), (14) *UAS-Tom20:3xHA* (F003545), (15) *UAS-Gapdh1:3xHA* (F002305), (16) *UAS-CkIIβ:3xHA* (F004937), (17) *UAS-Pex11:3xHA* (F004080), (18) *UAS-Atg18:3xHA* (F002805), (19) *UAS-Atg5:3xHA* (F003001), (20) *w; Atg9ᵈ⁵¹/CyO* (from GC. Chen; *Atg9* null), (21) *w; Atg9Gal4KO/CyO* (from G. C. Chen, Academia Sinica, Taipei, Taiwan; *Atg9* null) (22) *w; FIP200³ᶠ⁵/TM6B* (from J. H. Lee; *FIP200* null) (Kim et al., 2013), (23) *w; FIP200⁴ᴳ⁷/TM6B* (from J. H. Lee; *FIP200* null) (Kim et al., 2013), (24) *w; UAS-mCherry* (from A. Kiger, University of California, San Diego, USA) and (25) *w; P{w[+mC]=UAS-Rab5.S43N}2* (BL42703; UAS-Rab5ˢ⁴³ᴺ). New genotypes generated during this study include the following: (26) *w¹¹¹⁸; UAS-Spinster:3xHAᵃᵗᵗᴾ⁴⁰*, (27) *w¹¹¹⁸; UAS-Frankenbodyᴴᴬ:GFPᵃᵗᵗᴾ⁴⁰*, (28) *w¹¹¹⁸; UAS-Frankenbodyᴴᴬ:mCherry ᵃᵗᵗᴾ⁴⁰*, (29) *w¹¹¹⁸; UAS-Frankenbodyᴴᴬ:GFP:mCherry ᵃᵗᵗᴾ⁴⁰*, (30) *w¹¹¹⁸; QUAS-Frankenbodyᴴᴬ:GFPᵃᵗᵗᴾ²*, (31) *w¹¹¹⁸; QUAS-Frankenbodyᴴᴬ:mCherry ᵃᵗᵗᴾ²*, (32) *w¹¹¹⁸; QUAS-Frankenbodyᴴᴬ:GFP:mCherry ᵃᵗᵗᴾ²*, (33) *w¹¹¹⁸; UASt-HA-Frankenbody:GFP/CyO; pnr-GAL4/TM6c Sb Tb*, (34) *w¹¹¹⁸; UASt-HA-Frankenbody:GFP/CyO; DMef2-GAL4/TM6c Sb Tb*, (35) *w¹¹¹⁸; Cg-GAL4, UASt-HA-Frankenbody:GFP/CyO*, (36) *w¹¹¹⁸; UASt-HA-Frankenbody:mCherry/CyO; DMef2-GAL4/TM6c Sb Tb* and (37) *w¹¹¹⁸; Cg-GAL4, UASt-HA-Frankenbody:GFP:mCherry/CyO*.

Preparation of the fat body
Laid eggs were reared at 21°C on standard cornmeal/yeast/agar media for 21 h. Then they were reared at 25°C until they grew to 3IL or to white

prepupa. For nutrient starvation, 2IL larvae were transferred to fresh food and kept at 25°C for 24 h. The 3IL were reared in standard media (fed) or in 20% sucrose/PBS solution for 4 h (starved). For chloroquine feeding, laid eggs were grown in standard media with 3 mg/ml of chloroquine diphosphate until the indicated stage.

DNA engineering and generation of transgenic flies
Standard molecular biology techniques were used to construct plasmid vectors. The DNA polymerase KOD One (TOYOBO, Tokyo, Japan) was used for PCR amplification of all the objective sequences. For the expression vector of spinster-3xHA, the spinster coding sequence was amplified with the following primer set, 5′-CACCGAATTCACCATGTCGCTGAAACACCAGAAGCAATC-3′ and 5′-CTCGAGGGCAATCTGACCGCGGCTGATC-3′, from the cDNA. Amplified sequence was inserted into pENTR-D-TOPO vector with TOPO cloning (Thermo Fisher Scientific). The inserted coding sequence was transferred to the pTWH vector with the Gateway protocol using LR Clonase II Enzyme mix (Thermo Fisher Scientific). Construction of the expression vectors of C-terminal fluorescent protein-tagged HA Frankenbody under UAS control (pUASt-attB-Frankenbodyᴴᴬ-GFP, pUASt-attB- Frankenbodyᴴᴬ-mCherry, and pUASt-attB- Frankenbodyᴴᴬ-GFP-mCherry) was performed as follows: as a template, pCMV-15F11-HA-mEGFP was used (Zhao et al., 2019) and for pUASt-attB-Frankenbodyᴴᴬ-GFP, Frankenbodyᴴᴬ-GFP fragments were amplified with the following primer sets: 5′-ATAGGGAATTGGGAACACC-ATGGCCGAGGTGAAGCTGG-3′ and 5′-ACCCTCGAGCCGCGGC-TACTTGTACAGCTCGTCCATGCC-3′. For pUASt-attB- Frankenbodyᴴᴬ-mCherry, the fragments of Frankenbodyᴴᴬ and mCherry were amplified with the following primer sets: 5′-ATAGGGAATTGGGAACACCAT-GGCCGAGGTGAAGCTGG-3′ and 5′-ACCGCTTCCACCTCCACCGC-TTCCG-3′ for Frankenbodyᴴᴬ; and 5′-GGAGGTGGAAGCGGTATGGT-GAGCAAGGGCGAGGAGGA-3′ and 5′-TGGACGAGCTGTACAAGT-GACCGCGGCTCGAGGGT-3′ for mCherry. For pUASt-attB- Frankenbodyᴴᴬ -GFP-mCherry, the fragments of Frankenbodyᴴᴬ -GFP and mCherry were amplified with the following primer sets: 5′-ATAGGGAA-TTGGGAACACCATGGCCGAGGTGAAGCTGG-3′ and 5′-GCATG-GACGAGCTGTACAAGGGTGGACCG-3′ for Frankenbodyᴴᴬ -GFP; and 5′-ACAAGGGTGGACCGATGGTGAGCAAGGGCGAGGA-3′ and 5′-ATGGACGAGCTGTACAAGTGACCGCGGCTCGAGGGT-3′ for mCherry. Each set of fragments was assembled with pUASt-attB vector digested by EcoRI and NotI using Gibson assembly. The construction of the expression vectors of the C-terminal fluorescent-tagged Frankenbodyᴴᴬ under QUAS control (pQUASt-attB- Frankenbodyᴴᴬ-GFP, pQUASt-attB-Frankenbodyᴴᴬ-mCherry, pQUASt-attB- Frankenbodyᴴᴬ-GFP-mCherry) was performed as follows: the fragments of Frankenbodyᴴᴬ -GFP, Frankenbodyᴴᴬ -mCherry, and Frankenbodyᴴᴬ -GFP-mCherry were amplified with the following primer sets: 5′-GTTAGATCTCACCA-TGGCCGAGGTG-3′ and 5′-CTTCTCGAGCTACTTGTACAGCTCGTC-CATGCCGAG-3′ for Frankenbodyᴴᴬ -GFP; 5′-GTTAGATCTCACCA-TGGCCGAGGTG-3′ and 5′-CTTCTCGAGTCACTTGTACAGCTCGTC-CATGCCGCC-3′ for Frankenbodyᴴᴬ -mCherry; and 5′-GTTAGATCTC-ACCATGGCCGAGGTG-3′ and 5′-CTTCTCGAGTCACTTGTACA-GCTCGTCCATGCCGCC-3′ for Frankenbodyᴴᴬ -GFP-mCherry. The amplified fragments were purified and digested using BglII and XhoI. The digested DNA fragments were ligated to pQUASt-attB, also digested by BglII and XhoI using a Ligation-Convenience kit (NIPPON GENE). All the resultant vectors were validated by sequencing, and were then injected into embryos for P-element or phiC31 insertion (Wellgenetics).

Tissue preparation and immunofluorescence in *Drosophila*
Muscle preparations in larval fillets and pupal abdomens were performed as previously described (Ribeiro et al., 2011). 3IL or pupae were pinned on a sylgard-covered petri dish in dissection buffer [5 mM HEPES, 128 mM NaCl, 2 mM KCl, 4 mM MgCl₂ and 36 mM sucrose (pH 7.2)]. The animals were pinned flat and fixed at room temperature for 20 min (4% PFA, 50 mM EGTA in PBS). The samples were the unpinned and blocked at room temperature for 30 min (0.3% bovine serum albumin, 2% goat serum, 0.6% Triton X100 in PBS), incubated with primary antibody overnight at 4°C,

DEVELOPMENT

washed (0.1% Triton in PBS), then incubated with Alexa Fluor568-conjugated secondary antibody (Thermo Fisher Scientific) for 2 h at room temp. The immunostained samples were washed and mounted in FluorSave reagent (Merck Millipore). LEC preparations in 3IL larvae abdomens were performed as previously described (Tenenbaum and Gavis, 2016). After dissection and fixation, the larval body wall muscles were removed from the fillet using fine forceps. Samples were then unpinned and blocked at room temperature for 30 min (0.1% Triton X100, 0.3% BSA in PBS). Subsequent steps were performed as described above for muscles.

Fat body preparations in 3IL larvae were performed as follows. 3IL larvae were dissected with forceps in the dissection buffer. The fat bodies were fixed at room temperature for 20 min (4% PFA, 50 mM EGTA in PBS), blocked at room temperature for 30 min (1% Tween20, 2% BSA in PBS). Then the samples were incubated with primary antibody overnight at 4°C and incubated with Alexa Fluor405-conjugated secondary antibody (Thermo Fisher Scientific) for 2 h at room temp.

LysoTracker and LysoSensor staining of live fat body
Staged larvae were dissected in PBS, and a lobe of the fat body was collected. The fat bodies were stained with LysoTracker Red (1:10,000 in PBS for 2 min), Lysotracker Deep Red (1:1000 in PBS for 2 min) or LysoSensor Green (1:2000 in PBS for 2 min) at room temperature.

Magic Red staining of live fat body
Staged larvae were dissected in PBS with forceps. The collected fat body lobes were stained with Magic Red (1/250 in PBS) for 2 min at room temperature.

Confocal fluorescence microscopy
For imaging of live LECs, white prepupae were mounted between slide-glass and cover-glass with a spacer. For imaging of live LBWMs, third instar larvae were immobilized by making a tiny hole on the head with fine forceps in 4% PFA, and mounted between slide-glass and cover-glass with a spacer. Live fat bodies were mounted between slide-glass and cover-glass with PBS. LECs, LBWMs and fat bodies were observed on a confocal microscope FV3000 (Olympus) with a 60× silicone/1.30 NA UPlanSApo (Olympus). The image acquisition software used was Fluoview (Olympus). The exported images were adjusted and analyzed using ImageJ.

RNA-seq of fat body
Fat bodies were collected from staged five larvae or pupae. The isolated fat bodies were lysed in the TRIzol (Thermo Fisher Scientific) and frozen at −80°C. The lysates were quickly thawed and homogenized through a 27-gauge needle for 10 strokes. The total RNA was collected following the manufacturer's instructions. The samples were then further purified using ReliaPrep tissue RNA Miniprep System (Promega). cDNA libraries were constructed from the total RNAs using TruSeq stranded mRNA library platform (Illumina). The libraries were sequenced with paired-end sequencing by NovaSeq6000 (Illumina). The acquired FASTQ files were quantified using salmon (Patro et al., 2017) and statistical analysis was carried out of the fold change of the gene expression levels (early 3IL versus WP, or control at WP versus Mitf OE at WP) using R's Bioconductor plug-ins (DESeq2 with independent hypothesis weighting) (Love et al., 2014; Ignatiadis et al., 2016). The threshold of the adjusted P-value was set as 0.1.

Immunoblots
Fat bodies or whole larvae without gut were collected from three animals. The samples were lysed directly in 1.5× sample loading buffer [100 mM Tris-HCl (pH 6.8), 3% SDS, 15% glycerol and 0.03% Bromophenol Blue]. Equal amounts of proteins per sample were subjected to SDS-PAGE. The separated proteins were transferred to Immobilon-P^{SQ} PVDF transfer membrane (Merck Millipore) with Trans-Blot Turbo Transfer System (Bio-Rad). The membranes were blocked in blocking buffer [10 mM Tris-HCl (pH 8.0), 150 mM NaCl, 0.1% Tween 20 and 1% BSA] for 30 min, incubated with the primary antibodies in Can Get Signal Solution 1 (TOYOBO) overnight at 4°C and then incubated with secondary antibodies

in blocking buffer for 2 h at room temp. Immunoreactive bands were then detected using ECL plus (GE Healthcare Life Sciences) and FUSION (Vilber Lourmat). The images were processed using ImageJ.

Image analyses
We analyzed up to 10 images acquired from five lobes of the fat body from five animals for each experiment. For all analysis, images were cropped to 81.59×81.59 μm and were analyzed using ImageJ macro language. Below is the analysis process in brief. In Fig. 3C,E, Fig. S3B,E, the intensity of mCherry-only positive dots was quantified. The fluorescence intensity of the GFP channel in each pixel was subtracted from the corresponding pixel of mCherry intensity. The map was binarized and the mean intensity and area of each object was analyzed. In Fig. S4B, the area of bright spherical structures positive for both GFP and mCherry was quantified. Both GFP and mCherry channel images were binarized. They were then multiplied together to extract a double-positive area. The resultant map was used to analyze the area of each object. In Fig. 4C, the number of mCherry-positive and GFP-negative acidic compartments was counted using the same procedure as Fig. 3C,E and Fig. S3E. Both GFP- and mCherry-positive large objects were manually counted because it was challenging to segment them automatically. In Figs 4F,H, 6B and Fig. S6F, the mean intensity of Lysosensor Green of lamp-3xmCh-positive objects was quantified. First, the mCherry channel was binarized and filtered to exclude noise by size and circularity. Then, the mean intensity of Lysosensor Green was calculated for each binarized mCherry-positive object. In Fig. 5B, the number of GFP-Atg8-positive puncta was counted. The GFP channel image was binarized and filtered to remove noise. The number of small puncta was then counted. To measure the size of lysosomes in the 3IL fat body, the images were binarized and filtered to remove noise. The area of each object was then quantified. In the white prepupal fat body, lysosome size was analyzed manually using Fiji, because of the same issues with segmentation described above.

Statistics
Each experiment was performed at least three times and at least five different cohorts of unique flies were analyzed. All replicate experiments were performed in parallel with controls. Data are mean±s.d. When more than two genotypes or treatments were used in an experiment, the statistical analysis was performed using Tukey's test, Sidak's test or unpaired t-test on Prism8 and Prism9 software. A two-tailed unpaired Student's t-test was used to compare two means. $P<0.05$ was regarded as statistically significant (*$P<0.05$, **$P<0.001$, ***$P<0.0001$ and ****$P<0.00001$).

Author contributions
Conceptualization: T.M., N.F.; Methodology: T.M., N.F.; Software: T.M.; Validation: N.F.; Formal analysis: T.M., N.F.; Investigation: T.M., T.N., K.K., F.M., N.F.; Resources: T.M., N.Z., T.J.S., H.K., N.F.; Data curation: T.M., N.F.; Writing - original draft: N.F.; Writing - review & editing: T.M., K.K., T.J.S., H.K., N.F.; Visualization: N.F.; Supervision: N.F.; Funding acquisition: H.K., N.F.

References

Berry, D. L. and Baehrecke, E. H. (2007). Growth arrest and autophagy are required for salivary gland cell degradation in Drosophila. *Cell* **131**, 1137-1148. doi:10.1016/j.cell.2007.10.048

Bischof, J., Björklund, M., Furger, E., Schertel, C., Taipale, J. and Basler, K. (2012). A versatile platform for creating a comprehensive UAS-ORFeome library in Drosophila. *Development* **140**, 2434-2442. doi:10.1242/dev.088757

Bosch, J. A., Chen, C. L. and Perrimon, N. (2021). Proximity-dependent labeling methods for proteomic profiling in living cells: an update. *Wiley Interdiscip. Rev. Dev. Biol.* **10**, 1-17. doi:10.1002/wdev.392

Bouché, V., Espinosa, A. P., Leone, L., Sardiello, M., Ballabio, A. and Botas, J. (2016). Drosophila Mitf regulates the V-ATPase and the lysosomal-autophagic pathway. *Autophagy.* **12**, 484-498. doi:10.1080/15548627.2015.1134081

Brand, A. H. and Perrimon, N. (1993). Targeted gene expression as a means of altering cell fates and generating dominant phenotypes. *Development* **118**, 401-415. doi:10.1242/dev.118.2.401

Butterworth, F. M. and Forrest, E. C. (1984). Ultrastructure of the preparative phase of cell death in the larval fat body of Drosophila melanogaster. *Tissue Cell* **16**, 237-250. doi:10.1016/0040-8166(84)90047-8

Butterworth, F. M., Emerson, L. and Rasch, E. M. (1988). Maturation and degeneration of the fat body in the Drosophila larva and pupa as revealed by morphometric analysis. *Tissue Cell* **20**, 255-268. doi:10.1016/0040-8166(88)90047-X

Cherbas, L., Hu, X., Zhimulev, I., Belyaeva, E. and Cherbas, P. (2003). EcR isoforms in Drosophila: testing tissue-specific requirements by targeted blockade and rescue. *Development* **130**, 271-284. doi:10.1242/dev.00205

Collins, M. P. and Forgac, M. (2020). Regulation and function of V-ATPases in physiology and disease. *Biochim. Biophys. Acta Biomembr.* **1862**, 183341. doi:10.1016/j.bbamem.2020.183341

Dermaut, B., Norga, K. K., Kania, A., Verstreken, P., Pan, H., Zhou, Y., Callaerts, P. and Bellen, H. J. (2005). Aberrant lysosomal carbohydrate storage accompanies endocytic defects and neurodegeneration in Drosophila benchwarmer. *J. Cell Biol.* **170**, 127-139. doi:10.1083/jcb.200412001

Dunst, S. and Tomancak, P. (2019). Imaging flies by fluorescence microscopy: Principles, technologies, and applications. *Genetics.* **211**, 15-34. doi:10.1534/genetics.118.300227

Fujita, N., Huang, W., Lin, T.-H., Groulx, J.-F., Jean, S., Nguyen, J., Kuchitsu, Y., Koyama-Honda, I., Mizushima, N., Fukuda, M. et al. (2017). Genetic screen in drosophila muscle identifies autophagy-mediated T-tubule remodeling and a Rab2 role in autophagy. *eLife* **6**, e23367. doi:10.7554/eLife.23367

Guha, S., Coffey, E. E., Lu, W., Lim, J. C., Beckel, J. M., Laties, A. M., Boesze-Battaglia, K. and Mitchell, C. H. (2014). Approaches for detecting lysosomal alkalinization and impaired degradation in fresh and cultured RPE cells: evidence for a role in retinal degenerations. *Exp. Eye Res.* **126**, 68-76. doi:10.1016/j.exer.2014.05.013

Hegedűs, K., Takáts, S., Boda, A., Jipa, A., Nagy, P., Varga, K., Kovács, A. L. and Juhász, G. (2016). The Ccz1-Mon1-Rab7 module and Rab5 control distinct steps of autophagy. *Mol. Biol. Cell.* **27**, 3132-3142. doi:10.1091/mbc.e16-03-0205

Ignatiadis, N., Klaus, B., Zaugg, J. B. and Huber, W. (2016). Data-driven hypothesis weighting increases detection power in genome-scale multiple testing. *Nat. Methods.* **13**, 577-580. doi:10.1038/nmeth.3885

Johnson, A. E., Shu, H., Hauswirth, A. G., Tong, A. and Davis, G. W. (2015). VCP-dependent muscle degeneration is linked to defects in a dynamic tubular lysosomal network in vivo. *eLife* **4**, e07366. doi:10.7554/elife.07366

Kabeya, Y., Mizushima, N., Ueno, T., Yamamoto, A., Kirisako, T., Noda, T., Kominami, E., Ohsumi, Y. and Yoshimori, T. (2000). LC3, a mammalian homologue of yeast Apg8p, is localized in autophagosome membranes after processing. *EMBO J.* **19**, 5720-5728. doi:10.1093/emboj/19.21.5720

Kageyama, S., Gudmundsson, S. R., Sou, Y.-S., Ichimura, Y., Tamura, N., Kazuno, S., Ueno, T., Miura, Y., Noshiro, D., Abe, M. et al. (2021). p62/SQSTM1-droplet serves as a platform for autophagosome formation and anti-oxidative stress response. *Nat. Commun.* **12**, 16. doi:10.1038/s41467-020-20185-1

Kalvari, I., Tsompanis, S., Mulakkal, N. C., Osgood, R., Johansen, T., Nezis, I. P. and Promponas, V. J. (2014). iLIR: a web resource for prediction of Atg8-family interacting proteins. *Autophagy* **10**, 913-925. doi:10.4161/auto.28260

Kanca, O., Bellen, H. J. and Schnorrer, F. (2017). Gene tagging strategies to assess protein expression, localization, and function in Drosophila. *Genetics* **207**, 389-412. doi:10.1534/genetics.117.199968

Kim, M., Park, H. L., Park, H.-W., Ro, S.-H., Nam, S. G., Reed, J. M., Guan, J.-L. and Lee, J. H. (2013). Drosophila Fip200 is an essential regulator of autophagy that attenuates both growth and aging. *Autophagy* **9**, 1201-1213. doi:10.4161/auto.24811

Kim, M., Sandford, E., Gatica, D., Qiu, Y., Liu, X., Zheng, Y., Schulman, B. A., Xu, J., Semple, I., Ro, S.-H. et al. (2016). Mutation in ATG5 reduces autophagy and leads to ataxia with developmental delay. *eLife* **5**, e12245. doi:10.7554/elife.12245

Kimura, S., Noda, T. and Yoshimori, T. (2007). Dissection of the autophagosome maturation process by a novel reporter protein, tandem fluorescent-tagged LC3. *Autophagy* **3**, 452-460. doi:10.4161/auto.4451

Klionsky, D. J., Abdel-Aziz, A. K., Abdelfatah, S., Abdellatif, M., Abdoli, A., Abel, S., Abeliovich, H., Abildgaard, M. H., Abudu, Y. P., Acevedo-Arozena, A. et al. (2021). Guidelines for the use and interpretation of assays for monitoring autophagy (4th edition). *Autophagy* **17**, 1-382. doi:10.1080/15548627.2020.1797280

Komatsu, M., Waguri, S., Koike, M., Sou, Y.-S., Ueno, T., Hara, T., Mizushima, N., Iwata, J.-I., Ezaki, J., Murata, S. et al. (2007). Homeostatic levels of p62 control cytoplasmic inclusion body formation in autophagy-deficient mice. *Cell* **131**, 1149-1163. doi:10.1016/j.cell.2007.10.035

Love, M. I., Huber, W. and Anders, S. (2014). Moderated estimation of fold change and dispersion for RNA-seq data with DESeq2. *Genome Biol.* **15**, 550. doi:10.1186/s13059-014-0550-8

Mindell, J. A. (2012). Lysosomal acidification mechanisms for annual reviews in physiology. *Annu. Rev. Physiol.* **74**, 69-86. doi:10.1146/annurev-physiol-012110-142317

Mizushima, N., Noda, T., Yoshimori, T., Tanaka, Y., Ishii, T., George, M. D., Klionsky, D. J., Ohsumi, M. and Ohsumi, Y. (1998). A protein conjugation system essential for autophagy. *Nature.* **395**, 395-398. doi:10.1038/26506

Morishita, H. and Mizushima, N. (2019). Diverse Cellular Roles of Autophagy. *Annu. Rev. Cell Dev. Biol.* **35**, 453-475. doi:10.1146/annurev-cellbio-100818-125300

Murakawa, T., Kiger, A. A., Sakamaki, Y., Fukuda, M. and Fujita, N. (2020). An autophagy-dependent tubular lysosomal network synchronizes degradative activity required for muscle remodeling. *J. Cell Sci.* **133**, jcs248336. doi:10.1242/jcs.248336

Nezis, I. P., Simonsen, A., Sagona, A. P., Finley, K., Gaumer, S., Contamine, D., Rusten, T. E., Stenmark, H. and Brech, A. (2008). Ref(2)P, the Drosophila melanogaster homologue of mammalian p62, is required for the formation of protein aggregates in adult brain. *J. Cell Biol.* **180**, 1065-1071. doi:10.1083/jcb.200711108

Patro, R., Duggal, G., Love, M. I., Irizarry, R. A. and Kingsford, C. (2017). Salmon provides fast and bias-aware quantification of transcript expression using dual-phase inference. *Nat. Methods.* **14**, 417-419. doi:10.1038/nmeth.4197

Pircs, K., Nagy, P., Varga, A., Venkei, Z., Erdi, B., Hegedus, K. and Juhasz, G. (2012). Advantages and limitations of different p62-based assays for estimating autophagic activity in Drosophila. *PLoS ONE* **7**, e44214. doi:10.1371/journal.pone.0044214

Riabinina, O., Luginbuhl, D., Marr, E., Liu, S., Wu, M. N., Luo, L. and Potter, C. J. (2015). Improved and expanded Q-system reagents for genetic manipulations. *Nat. Methods* **12**, 219-222. doi:10.1038/nmeth.3250

Ribeiro, I., Yuan, L., Tanentzapf, G., Dowling, J. J. and Kiger, A. (2011). Phosphoinositide regulation of integrin trafficking required for muscle attachment and maintenance. *PLoS Genet.* **7**, e1001295. doi:10.1371/journal.pgen.1001295

Richter, K. N., Revelo, N. H., Seitz, K. J., Helm, M. S., Sarkar, D., Saleeb, R. S., D'Este, E., Eberle, J., Wagner, E., Vogl, C. et al. (2018). Glyoxal as an alternative fixative to formaldehyde in immunostaining and super-resolution microscopy. *EMBO J.* **37**, 139-159. doi:10.15252/embj.201695709

Rigon, L., De Filippis, C., Napoli, B., Tomanin, R. and Orso, G. (2021). Exploiting the potential of drosophila models in lysosomal storage disorders: Pathological mechanisms and drug discovery. *Biomedicines* **9**, 268. doi:10.3390/biomedicines9030268

Rusten, T. E., Lindmo, K., Juhász, G., Sass, M., Seglen, P. O., Brech, A. and Stenmark, H. (2004). Programmed autophagy in the Drosophila fat body is induced by ecdysone through regulation of the PI3K Pathway. *Dev. Cell.* **7**, 179-192. doi:10.1016/j.devcel.2004.07.005

Sillence, D. J. (2013). Glucosylceramide modulates endolysosomal pH in Gaucher disease. *Mol. Genet. Metab.* **109**, 194-200. doi:10.1016/j.ymgme.2013.03.015

Song, P., Li, S., Wu, H., Gao, R., Rao, G., Wang, D., Chen, Z., Ma, B., Wang, H., Sui, N. et al. (2016). Parkin promotes proteasomal degradation of p62: implication of selective vulnerability of neuronal cells in the pathogenesis of Parkinson's disease. *Protein Cell* **7**, 114-129. doi:10.1007/s13238-015-0230-9

Tenenbaum, C. M. and Gavis, E. R. (2016). Removal of drosophila muscle tissue from larval fillets for immunofluorescence analysis of sensory neurons and epidermal cells. *J. Vis. Exp.* **2016**, 1-8. doi:10.3791/54670

DEVELOPMENT

Vandemoortele, G., Eyckerman, S. and Gevaert, K. (2019). Pick a tag and explore the functions of your pet protein. *Trends Biotechnol.* **37**, 1078-1090. doi:10.1016/j.tibtech.2019.03.016

Venken, K. J. T. and Bellen, H. J. (2014). Chemical mutagens, transposons, and transgenes to interrogate gene function in Drosophila melanogaster. *Methods* **68**, 15-28. doi:10.1016/j.ymeth.2014.02.025

Wen, J.-K., Wang, Y.-T., Chan, C.-C., Hsieh, C.-W., Liao, H.-M., Hung, C.-C. and Chen, G.-C. (2017). Atg9 antagonizes TOR signaling to regulate intestinal cell growth and epithelial homeostasis in Drosophila. *eLife* **6**, 1-22. doi:10.7554/eLife.29338

Zhang, T., Zhou, Q., Ogmundsdottir, M. H., Möller, K., Siddaway, R., Larue, L., Hsing, M., Kong, S. W., Goding, C. R., Palsson, A. et al. (2015). Mitf is a master regulator of the v-ATPase, forming a control module for cellular homeostasis with v-ATPase and TORC1. *J. Cell Sci.* **128**, 2938-2950. doi:10.1242/jcs.173807

Zhao, N., Kamijo, K., Fox, P. D., Oda, H., Morisaki, T., Sato, Y., Kimura, H. and Stasevich, T. J. (2019). A genetically encoded probe for imaging nascent and mature HA-tagged proteins in vivo. *Nat. Commun.* **10**, 2947. doi:10.1038/s41467-019-10846-1

Zhou, W., Wang, H., Yang, Y., Chen, Z.-S., Zou, C. and Zhang, J. (2020). Chloroquine against malaria, cancers and viral diseases. *Drug Discov. Today* **25**, 2012-2022. doi:10.1016/j.drudis.2020.09.010
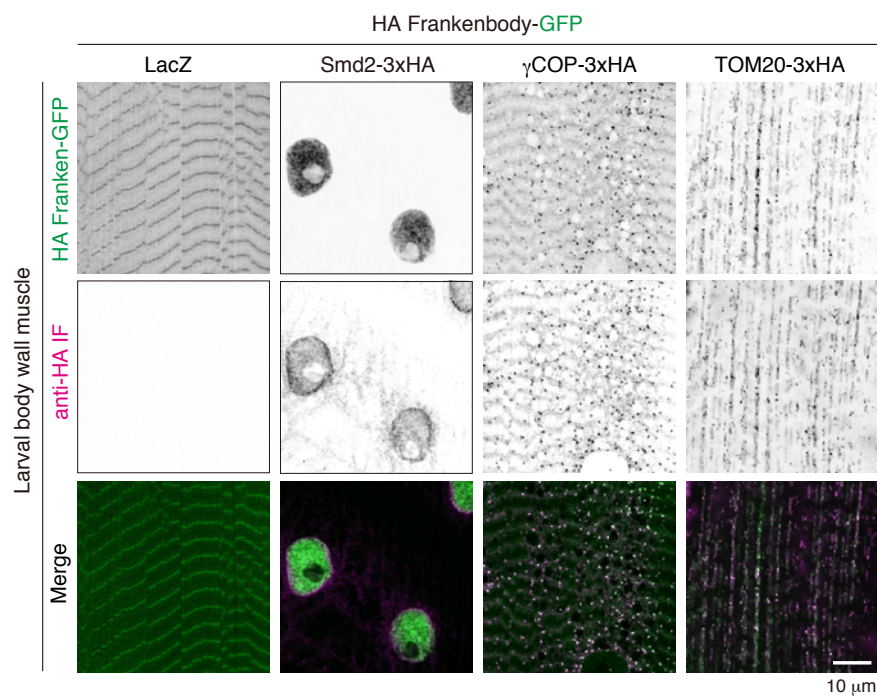
DEVELOPMENT

Fig. S1. HA Frankenbody recognizes HA-tagged protein in the larval body wall muscles

Colocalization of HA Frankenbody-GFP and anti-HA immunostaining of LacZ, Smd2-3xHA γCOP-3xHA, or TOM20-3xHA in third instar larval body wall muscles.
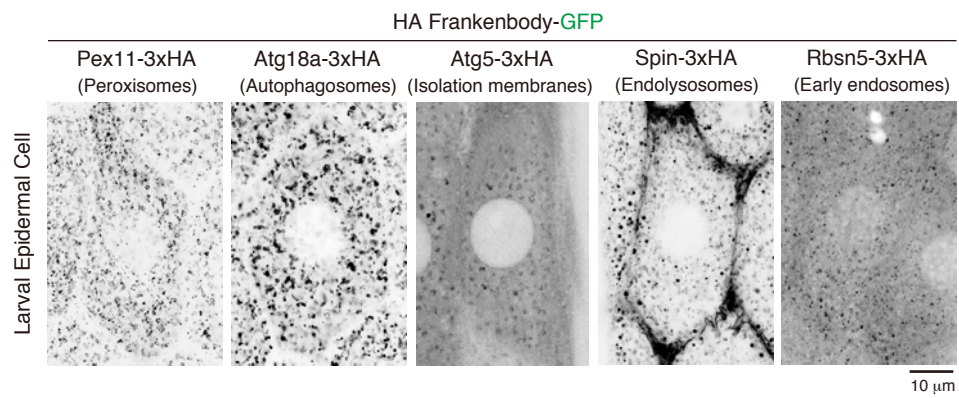
Fig. S2. HA Frankenbody allows imaging of HA-tagged constructs in live LECs

Localization of HA Frankenbody-GFP in cells expressing a series of 3xHA-tagged proteins in live LECs.
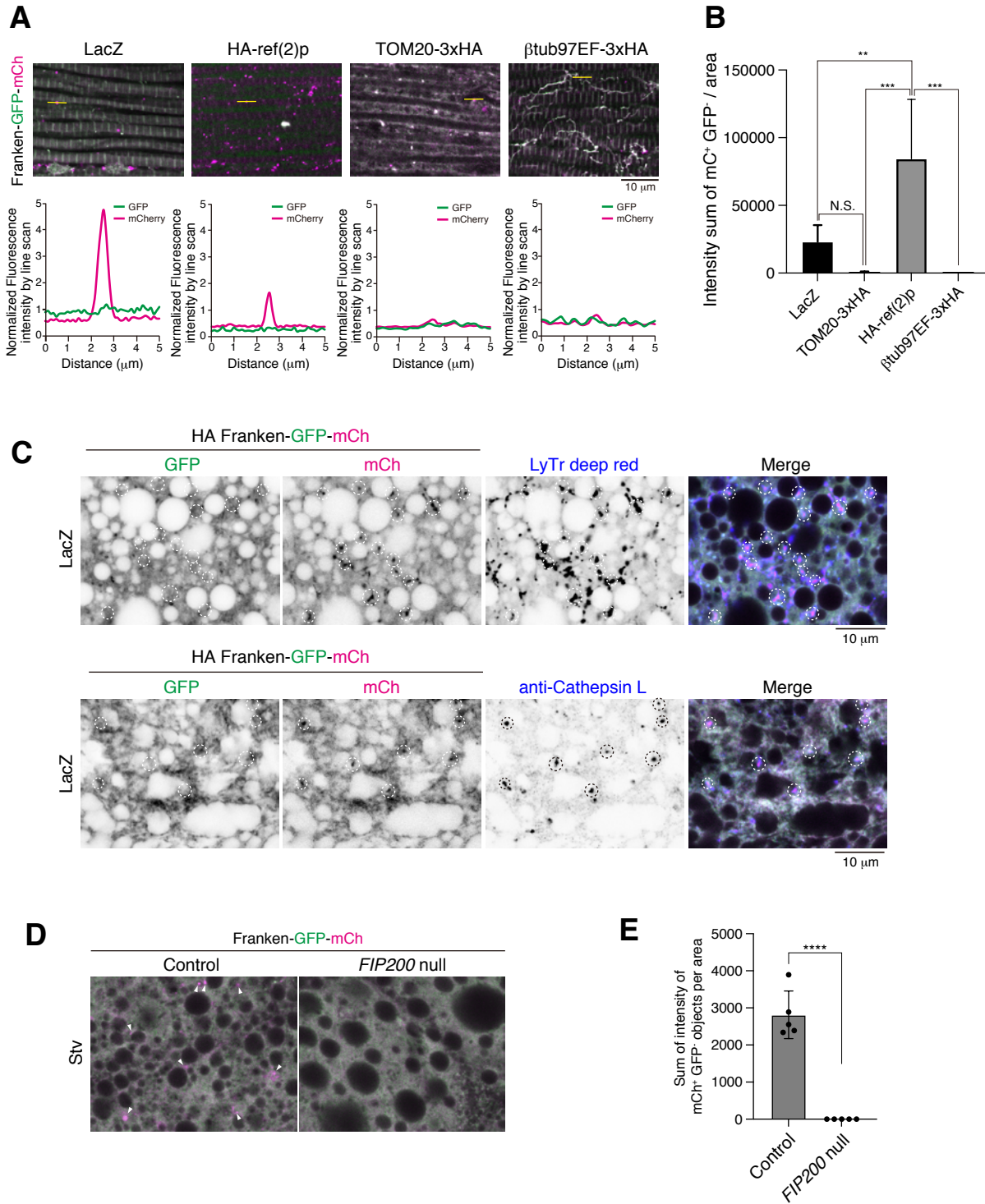
Fig. S3. Autophagic degradation of HA-tagged constructs

(A and B) Indirect flight muscles expressing HA Frankenbody-GFP-mCh and HA-tagged indicated constructs at 1-week-old adult. (A) Confocal images of GFP and mCh channels in the indicated conditions (upper row). Line plots profile the yellow line in each panel (lower row). (B) Quantification of the total intensity of mCh-positive and GFP-negative objects per area; ±SD for 5 images from 5 animals. (C) Colocalization of HA Frankenbody-GFP-mCh and LysoTracker Deep Red (Top) or Cathepsin L (Bottom) in starved early third instar larval fat body. (D and E) Loss of *FIP200* on the degradation of HA Frankenbody-GFP-mCh in the 3IL fat body. (D) Confocal images of GFP and mCh in control or *FIP200* null. (E) Quantification of the total intensity of mCh-positive and GFP-negative objects per area; ±SD for 5 images from 5 animals.
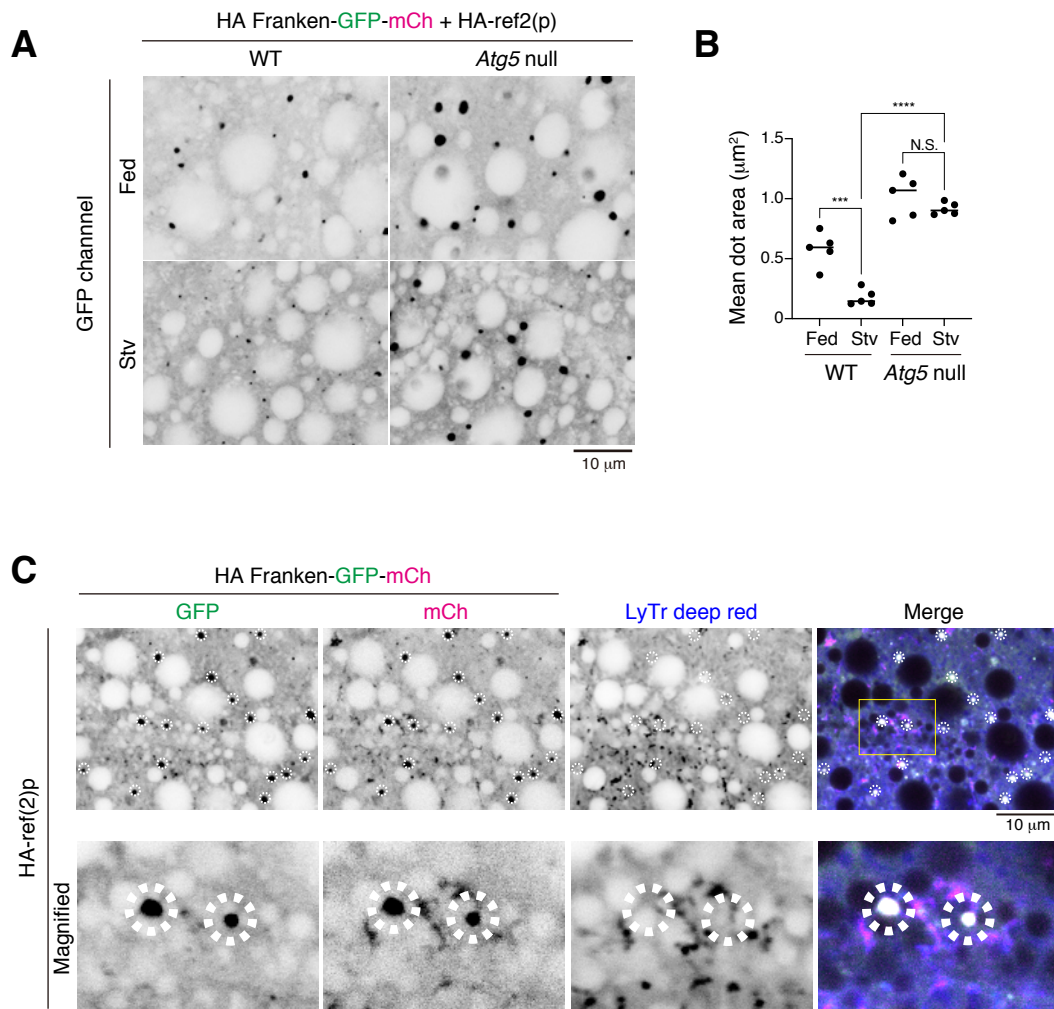
Fig. S4. The spherical ref(2)p droplets are not acidic compartments

(A and B) Loss of *Atg5* on the ref(2)p droplets in the fat body co-expressing HA-ref(2)p and HA Frankenbody-GFP-mCh. (A) Confocal images of GFP channel in the indicated conditions. (B) Mean area of GFP-positive dots; ±SD for 5 images from 5 animals. (C) LysoTracker Deep Red staining of fed 3IL fat bodies expressing both HA Frankenbody-GFP-mCh and HA-ref(2)p. White dotted circles show HA Frankenbody-GFP-mCh-positive ref(2)p droplets.
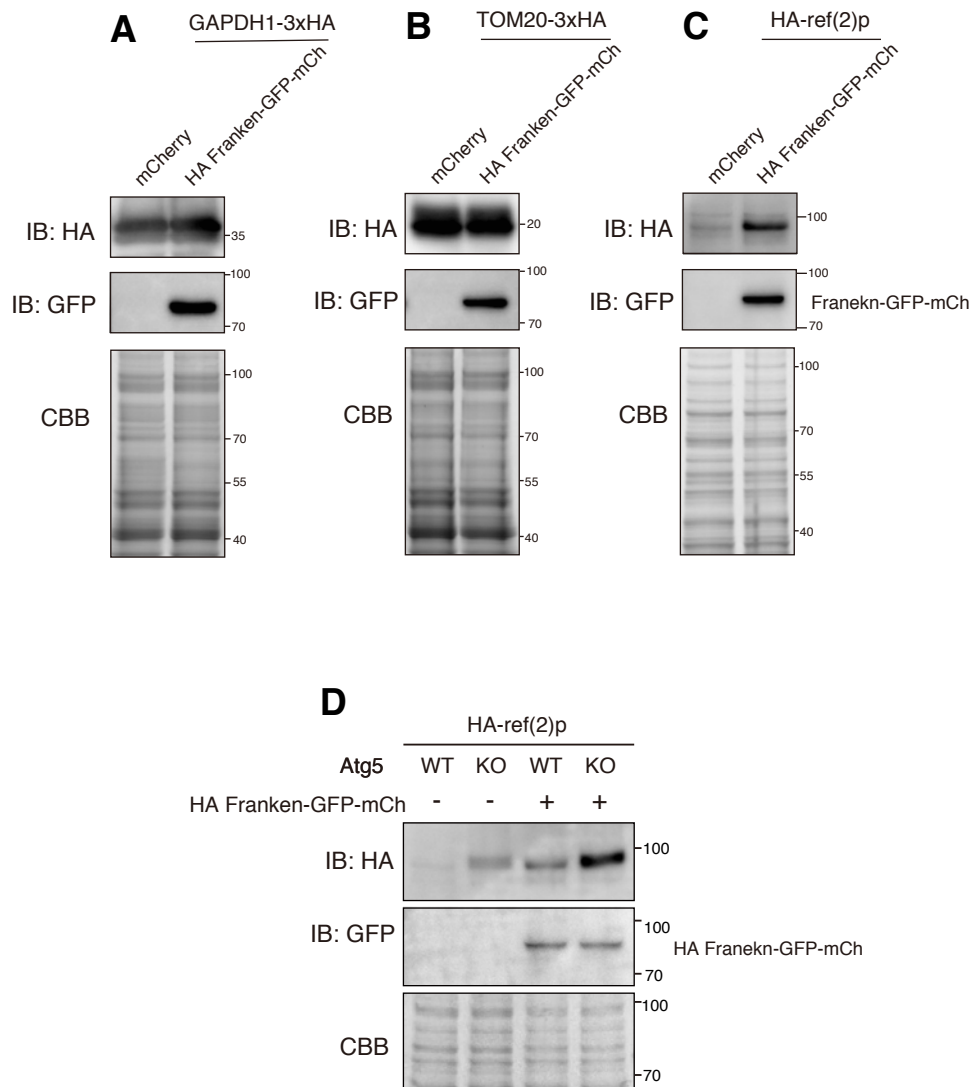
Fig. S5. HA Frankenbody-TF did not trigger degradation of HA-fused constructs
(A-C) Effect of HA Frankenbody-TF expression on the protein level of GAPDH-3xHA
(A), TOM20-3xHA (B), or HA-ref(2)p in larval fat bodies. The 3rd instar larvae
expressing mCherry (control) or HA Frankenbody-TF were starved for 4 h and
dissected. Western blotting was performed using the indicated antibodies. (D)
Elevation of HA-ref(2)p protein level by HA Frankenbody-TF expression was
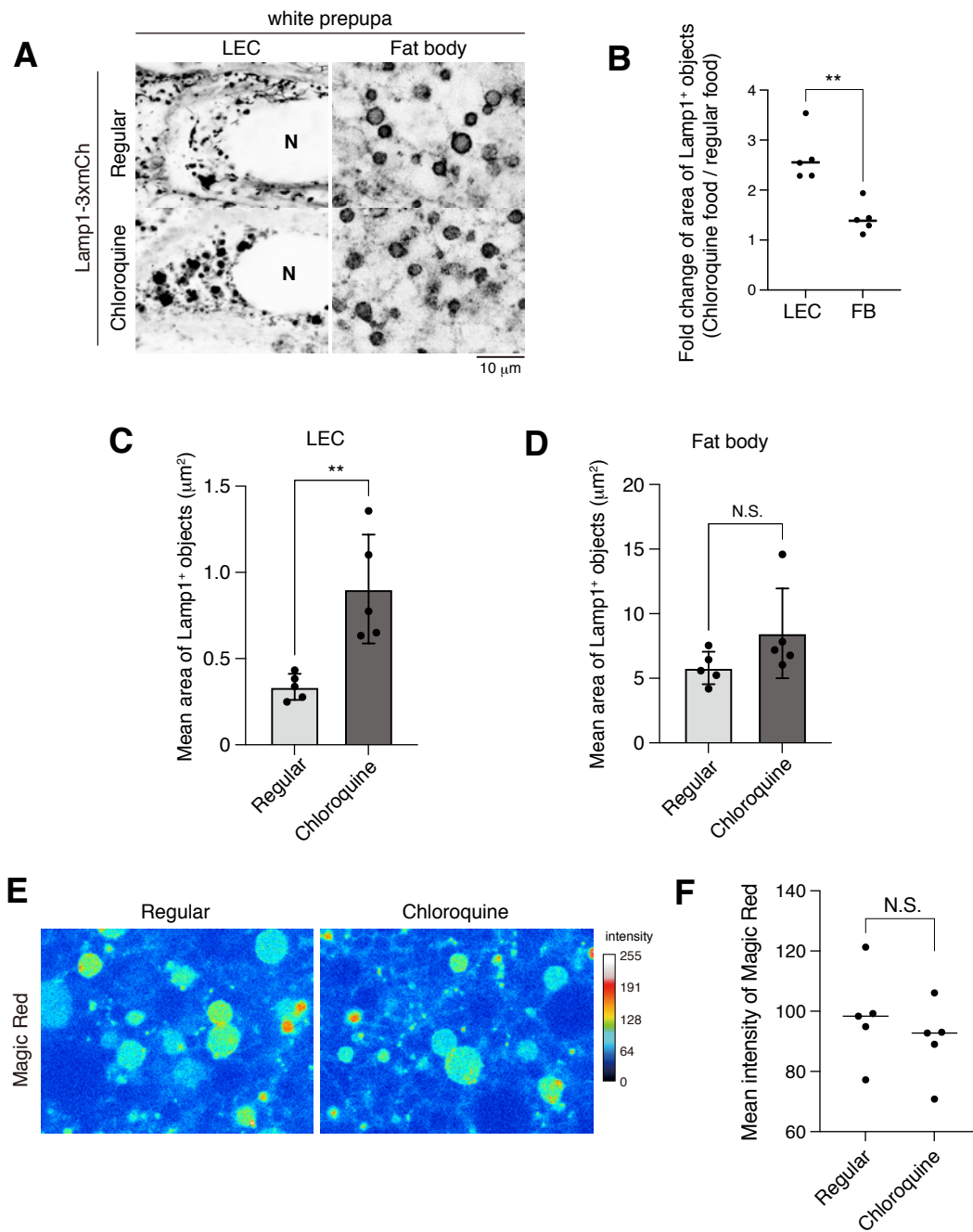independent of *Atg5*.

Fig. S6. Chloroquine feeding on lysosomal swelling in the white prepupal fat body

(A-D) Chloroquine feeding on the size of lysosomes in LECs or fat bodies at pupariation, N; nucleus. (A) Confocal images of Lamp1-3xmCh under the indicated conditions. (B) Fold change of the area of Lamp1-3xmCh-positive lysosomes upon chloroquine feeding. (C) Mean area of Lamp1-3xmCh-positive lysosomes in white prepupal LECs raised in regular or chloroquine food. N=5. (D) Mean area of Lamp1-3xmCh-positive lysosomes in white prepupal fat bodies raised in regular or chloroquine food. N=5. (E and F) Chloroquine feeding on lysosomal activity. (E) Fat bodies were stained with MagicRed under the indicated condition at pupariation (white prepupa). The intensity map shows a representative image of the intensities of MagicRed-positive objects. (F) Quantification of mean intensities of MagicRed-positive objects. N=5.
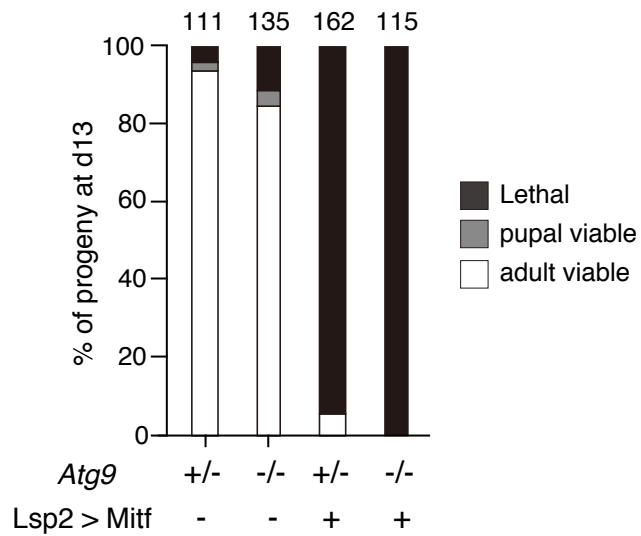
Fig. S7. Autophagy is indispensable for the Mitf overexpression-induced lethality

Percentage of viable and lethal progeny at 13 days after egg laying with fat body-targeted Mitf overexpression in the presence or absence of *Atg9*.

Table S1. Detailed *Drosophila* genotypes shown in figures

	Panel #	Genotype	Stage	Temp (˚C)
Figure 1	1B	*UAS-Franken:GFP/UAS-LacZ; pnr-GAL4/+*	3IL	25˚C
		UAS-Franken:GFP/+; pnr-GAL4/UAS-γCOP:3xHA	3IL	25˚C
		UAS-Franken:GFP/+; pnr-GAL4/UAS-Tom20:3xHA	3IL	25˚C
		UAS-Franken:GFP/+; pnr-GAL4/UAS-βTub97EF:3xHA	3IL	25˚C
Figure 2	2A	*UAS-Franken:GFP/UAS-LacZ; pnr-GAL4/+*	white prepupa	25˚C
		UAS-Franken:GFP/+; pnr-GAL4/UAS-SmD2:3xHA	white prepupa	25˚C
		UAS-Franken:GFP/+; pnr-GAL4/UAS-γCOP:3xHA	white prepupa	25˚C
		UAS-Franken:GFP/+; pnr-GAL4/UAS-Tom20:3xHA	white prepupa	25˚C
		UAS-Franken:GFP/+; pnr-GAL4/UAS-bTub97EF:3xHA	white prepupa	25˚C
	2B	*UAS-Franken:GFP/UAS-LacZ; DMef2-GAL4/+*	3IL	25˚C
		UAS-Franken:GFP/+; DMef2-GAL4/UAS-SmD2:3xHA	3IL	25˚C
		UAS-Franken:GFP/+; DMef2-GAL4/UAS-γCOP:3xHA	3IL	25˚C
		UAS-Franken:GFP/+; DMef2-GAL4/UAS-Tom20:3xHA	3IL	25˚C
		UAS-Franken:GFP/+; DMef2-GAL4/UAS-βTub97EF:3xHA	3IL	25˚C
	2C	*UAS-Franken:GFP, Cg-GAL4/UAS-LacZ; +/+*	3IL	25˚C
		UAS-Franken:GFP, Cg-GAL4/+; +/UAS-SmD2:3xHA	3IL	25˚C
		UAS-Franken:GFP, Cg-GAL4/+; +/UAS-γCOP:3xHA	3IL	25˚C
		UAS-Franken:GFP, Cg-GAL4/+; +/UAS-Tom20:3xHA	3IL	25˚C
		UAS-Franken:GFP, Cg-GAL4/+; +/UAS-βTub97EF:3xHA	3IL	25˚C
	2D	*UAS-Franken:mCh/UAS-Spinster:3xHA; DMef2-GAL4/+*	20 h APF	18˚C
Figure 3	3B	*UAS-Franken:GFP:mCh, Cg-GAL4/UAS-LacZ; +/+*	early 3IL	25˚C
		UAS-Franken:GFP:mCh, Cg-GAL4/+; +/UAS-GAPDH1:3xHA	early 3IL	25˚C
		UAS-Franken:GFP:mCh, Cg-GAL4/+; +/UAS-TOM20:3xHA	early 3IL	25˚C
		UAS-Franken:GFP:mCh, Cg-GAL4/+; +/UAS-HA:ref(2)p	early 3IL	25˚C
	3D	*w[1118]/Y; UAS-Franken:GFP:mCh, Cg-GAL4/+; UAS-HA:ref(2)p/+*	early 3IL	25˚C
		Atg5[5cc5]/Y; UAS-Franken:GFP:mCh, Cg-GAL4/+; UAS-HA:ref(2)p/+	early 3IL	25˚C
Figure 4	4B	*UAS-Franken:GFP:mCh, Cg-GAL4/+; +/UAS-GAPDH1:3xHA*	early 3IL, white prepupa	25˚C
		UAS-Franken:GFP:mCh, Cg-GAL4/+;+/UAS-CK2β:3xHA	early 3IL, white prepupa	25˚C
		UAS-Franken:GFP:mCh, Cg-GAL4/+; +/UAS-HA:ref(2)p	early 3IL, white prepupa	25˚C
	4D	*UAS-Franken:GFP:mCh, Cg-GAL4/+; +/UAS-HA:ref(2)p*	white prepupa	25˚C
	4E	*endo_promoter-Lamp1:3xmCherry[1-9M] /CyO*	early 3IL, white prepupa	25˚C
	4G	*w[1118]; +/+; +/+*	early 3IL, white prepupa	25˚C
Figure 5	5A	*w; Cg-GAL4/UAS-GFP:Atg8; +/+*	early 3IL, white prepupa	25˚C
	5E	*w[1118]/Y; +/endo_promoter-Lamp1:3xmCherry[1-9M]; UAS-HA:ref(2)p/+*	early 3IL, white prepupa	25˚C
		Atg5[5cc5]/Y; +/endo_promoter-Lamp1:3xmCherry[1-9M]; UAS-HA:ref(2)p/+	early 3IL, white prepupa	25˚C
	5G	*w/Y; +/+; +/+*	white prepupa	25˚C
		Atg5[5cc5]/Y; +/+; +/+	white prepupa	25˚C
		FIP200[3F5]/FIP200[4G7]	white prepupa	25˚C
		UAS-Rab5[S43N]/+; Lsp2-GAL4/+	white prepupa	25˚C
	5H	*w/Y; +/+; +/+*	white prepupa	25˚C
		Atg5[5cc5]/Y; +/+; +/+	white prepupa	25˚C
	5I	*FIP200[3F5]/FIP200[4G7]*	white prepupa	25˚C
		FIP200[4G7]/+	white prepupa	25˚C
	5J	*UAS-LacZ/+; Lsp2-GAL4/+*	white prepupa	25˚C
		UAS-Rab5[S43N]/+; Lsp2-GAL4/+	white prepupa	25˚C
Figure 6	6A	*UAS-LacZ/endo_promoter-Lamp1:3xmCherry[1-9M;] Lsp2-GAL4/+*	white prepupa	25˚C
		UAS-Mitf/endo_promoter-Lamp1:3xmCherry[1-9M]; Lsp2-GAL4/+	white prepupa	25˚C

6C		UAS-LacZ/+; Lsp2-GAL4/+	white prepupa	25˚C
		UAS-Mitf/+; Lsp2-GAL4/+	white prepupa	25˚C
6E		UAS-LacZ/+; Lsp2-GAL4/+	at day13	25˚C
		UAS-Mitf/+; Lsp2-GAL4/+	at day13	25˚C
6F		UAS-LacZ/+; Lsp2-GAL4/+	3IL	25˚C
		UAS-LacZ/+; Lsp2-GAL4/+	white prepupa	25˚C
		UAS-Mitf/+; Lsp2-GAL4/+	white prepupa	25˚C
Figure S1		UAS-Franken:GFP/UAS-LacZ; DMef2-GAL4/+	3IL	25˚C
		UAS-Franken:GFP/+; DMef2-GAL4/UAS-SmD2:3xHA	3IL	25˚C
		UAS-Franken:GFP/+; DMef2-GAL4/UAS-γCOP:3xHA	3IL	25˚C
		UAS-Franken:GFP/+; DMef2-GAL4/UAS-Tom20:3xHA	3IL	25˚C
Figure S2		UAS-Franken:GFP/+; pnr-GAL4/UAS-Pex11:3xHA	white prepupa	25˚C
		UAS-Franken:GFP/+; pnr-GAL4/UAS-Atg18a:3xHA	white prepupa	25˚C
		UAS-Franken:GFP/+; pnr-GAL4/UAS-Atg5:3xHA	white prepupa	25˚C
		UAS-Franken:GFP/+; pnr-GAL4/UAS-Spin:3xHA	white prepupa	25˚C
		UAS-Franken:GFP/+; pnr-GAL4/UAS-bTub97EF:3xHA	white prepupa	25˚C
Figure S3	S3A	UAS-Franken:GFP:mCh, Cg-GAL4/UAS-LacZ; +/+	early 3IL	25˚C
	S3B	w; UAS-Franken:GFP:mCh/UAS-LacZ; , DMef2-GAL4/+	1-week-old adult	25˚C
		w; UAS-Franken:GFP:mCh/+; DMef2-GAL4/UAS-HA:ref(2)p	1-week-old adult	25˚C
		w; UAS-Franken:GFP:mCh/+; DMef2-GAL4/UAS-TOM20:3xHA	1-week-old adult	25˚C
		w; UAS-Franken:GFP:mCh/+; DMef2-GAL4/UAS-βtub97EF:3xHA	1-week-old adult	25˚C
	S3D	Cg-GAL4, UAS-Franken:GFP:mCh/+; FIP200^{3F5}/+	early 3IL	25˚C
		Cg-GAL4, UAS-Franken:GFP:mCh/+; FIP200^{3F5}/FIP200^{4G7}	early 3IL	25˚C
Figure S4	S4A	w^{1118}/Y; UAS-Franken:GFP:mCh, Cg-GAL4/+; UAS-HA:ref(2)p/+	early 3IL	25˚C
		Atg5^{5cc5}/Y; UAS-Franken:GFP:mCh, Cg-GAL4/+; UAS-HA:ref(2)p/+	early 3IL	25˚C
	S4C	UAS-Franken:GFP:mCh, Cg-GAL4/+; +/UAS-HA:ref(2)p	early 3IL	25˚C
Figure S5	S5A	Cg-GAL4, UAS-mCherry/+; +/UAS-GAPDH1:3xHA	early 3IL	25˚C
		Cg-GAL4, UAS-Franken:GFP:mCherry/+; +/UAS-GAPDH1:3xHA	early 3IL	25˚C
	S5B	Cg-GAL4, UAS-mCherry/+; +/UAS-TOM20:3xHA	early 3IL	25˚C
		Cg-GAL4, UAS-Franken:GFP:mCherry/+; +/UAS-TOM20:3xHA	early 3IL	25˚C
	S5C	Cg-GAL4, UAS-mCherry/+; +/UAS-HA:ref(2)p	early 3IL	25˚C
		Cg-GAL4, UAS-Franken:GFP:mCherry/+; +/UAS-HA:ref(2)p	early 3IL	25˚C
	S5D	w/Y; Cg-GAL4/+; +/UAS-HA:ref(2)p	early 3IL	25˚C
		Atg5^{5cc5}/Y; Cg-GAL4/+; +/UAS-HA:ref(2)p	early 3IL	25˚C
		w/Y; +/Cg-GAL4, UAS-Franken:GFP:mCherry; +/UAS-HA:ref(2)p	early 3IL	25˚C
		Atg5^{5cc5}/Y; +/Cg-GAL4, UAS-Franken:GFP:mCherry; +/UAS-HA:ref(2)p	early 3IL	25˚C
Figure S6	S6A	endo_promoter-Lamp1:3xmCherry1-9M /CyO	white prepupa	25˚C
	S6E	w^{1118}; +/+; +/+		
Figure S7		Atg9^{GAL4KO}/+; Lsp2-GAL4/+	at day13	25˚C
		Atg9^{GAL4KO}/Atg9^{d51}; Lsp2-GAL4/+	at day13	25˚C
		Atg9^{GAL4KO}/+; Lsp2-GAL4/UAS-Mitf	at day13	25˚C
		Atg9^{GAL4KO}/Atg9^{d51}; Lsp2-GAL4/UAS-Mitf	at day13	25˚C